Novel $MgFe_2O_4$-CuO/GO heterojunction magnetic nanocomposite: Synthesis, characterization, and batch photocatalytic degradation of methylene blue dye

Ibrahim F. Waheed[1], Omer Yasin Thayee Al-Janabi[2*], Peter J. S. Foot[3]

[1]College of Science, Industrial Chemistry, Tikrit University, Salah Aldeen, Tikrit 34001, Iraq

[2]College of Petroleum Processes Engineering, Petroleum & Gas Refining Engineering, Tikrit University, Salah Aldeen, Tikrit 34001, Iraq

[3]Kingston University London, School of LSPC, Kingston upon Thames KT1 2EE (UK)

*corresponding author: omaroilgas@tu.edu.iq

Abstract

Methylene blue (MB) utilized in chemical industries and research laboratories, produces a considerable amount of wastewater and causes water pollution even at low concentration. In the present work, novel low bandgap $MgFe_2O_4$-CuO/graphene oxide nanocomposite was used as a heterojunction magnetic nanophotocatalyst to photodegrade MB in simulated wastewater. The photocatalyst was synthesized via a microwave-ultrasonic route and characterized by a group of spectroscopic techniques. The synthesized photocatalyst had a specific surface area of 96.12 $m^2.g^{-1}$, pore volume of 0.0521 $cm^3.g^{-1}$, and pore diameter of 2.90 nm. Batch photocatalytic degradation of MB dye was performed at 25°C under ambient sunlight, and carefully optimized to obtain maximum photodegradation efficiency. Under optimal conditions, the synthesized photocatalyst demonstrated superior degradation efficiency reaching 98.8% within 27 minutes. Recyclability studies showed that the synthesized photocatalyst had a very good stability and reusability up to four cycles.

Keywords: Semiconductor alloy; Heterojunction; Magnetic nanocomposite; Photocatalyst; MB degradation

1. Introduction

Organic dye industry effluents like methylene blue dye (MB) which has a non-biodegradable aromatic structure and absorbs the majority of sunlight radiation, accumulates in wastewater and causes serious damage to marine ecosystems and human life [1-5]. As a result, the elimination of such dyes from wastewater has become a priority for many researchers worldwide [6-10]. To date, a number of techniques have been developed to eliminate organic dyes from industrial effluents, including adsorption [11, 12], membrane technology [13], photocatalysis [14] and more [15-18]. Among all these approaches, photocatalysis has received huge interest in recent decades due to its low cost, nontoxic nature, ease of execution, low energy consumption and ability to be reused [19-22]. Photocatalytic water treatment is a well-known and eco-friendly advanced oxidation process (AOP) which involves a photochemical reaction on the surface of a photocatalyst that produces electron-hole pairs when

exposed to light. The electron-hole pairs facilitate the degradation of complex organic pollutants, mainly to CO_2, H_2O and other innocuous inorganic materials [23, 5]. Semiconductor-mediated photocatalysis has sparked a lot of interest due to its potency to photodegrade a vast range of organic and inorganic pollutants under ambient conditions without toxic by-products [24]. Semiconductor photocatalysts can be excited to an energy level higher than their bandgap, inducing the generation of energy-rich photo-carriers, which can be involved in redox reactions to decompose organic dyes [25-28]. The effectiveness of such processes is inextricably linked to the transport of the photogenerated carriers which is influenced by the materials' morphology, particle size, size distribution, dosage, pollutant concentration and pH [29, 30].

Because of their excellent photocatalytic properties and ease of fabrication, narrow bandgap semiconductors such as spinel ferrite nanoparticles with formula MFe_2O_4 (M: Mn, Zn, Co, Mg, Ni, etc.) have been selected as versatile nominees for diverse applications, including pollution control [31-36]. Another useful feature is their magnetic property which facilitates the process of separating them from the polluted aqueous solution by applying an external magnetic field. They can also be reused, which is a key feature of wastewater treatment technology [37-39]. A major drawback of spinel ferrite nanoparticles is the formation of agglomerates during synthesis as a result of magnetic interaction, which can reduce the active surface area and thus the degradation performance [40]. Moreover, fast electron-hole recombination rates diminish their photo-degradation efficiency under visible light irradiation. Therefore, many attempts were made to address these problems by metal doping [41-43].

In this work, we have engineered a novel heterojunction photocatalyst capable of overcoming the above disadvantages and degrading persistent contaminants such as organic dyes, which are not naturally degraded in the environment. Our heterojunction photocatalyst was manufactured using a semiconductor alloy composed of magnesium ferrite $MgFe_2O_4$ (MFO) and copper oxide (CuO), on a substrate of graphene oxide (GO) nano-sheets. GO-based composite materials have unique chemical, mechanical and electrical properties as well as large specific surface area and good adsorption capability, making them powerful competitor photocatalysts for visible light-driven photodegradation of organic pollutants [44, 45]. MFO n-type semiconductor is a promising UV-visible absorber with a narrow bandgap and a soft magnetic nature that aids its separation from aqueous systems [46-48]. Furthermore, MFO has good photostability in both alkaline and acidic solutions, rendering it an ideal candidate for environmental remediation. Copper oxide CuO p-type, on the other hand, has superior photoconductive as well as photochemical properties, narrow bandgap and low bulk density [49]. It has a large surface area and porosity, and when exposed to solar radiation, it can exhibit strong absorption in the visible region [50]. In this study, GO nano-sheets were incorporated into $MgFe_2O_4$-CuO semiconductor alloy as a support for the active materials and to hinder agglomeration during

synthesis, effectively promote charge separation and extend the lifetime of the charge carriers for improved photocatalytic efficiency. Microwave-ultrasonic route is widely used technique to create the conditions for rapid and intimate reaction in nanoscale and colloidal systems; the ultrasonication produces excellent agitation and transient local heating, which is supported by the microwave energy input. For the above features, a microwave-assisted approach was chosen to synthesize our $MgFe_2O_4$-CuO decorated GO nano-sheets nanocomposite. The synthesized MFO-CuO@GO nanocomposite was characterized using XRD, FTIR, Raman spectroscopy and energy dispersive X-ray analysis (EDX). Field emission scanning electron microscopy (FE-SEM) was used to investigate surface morphology, while particle sizes were inspected by transmission electron microscopy (TEM). The Brunauer-Emmett-Teller (BET) method was used to determine the specific surface area and pore size distribution of the prepared $MgFe_2O_4$-CuO/GO hetero-junction photocatalyst, as well as pore volumes using the Barret-Joyner-Halenda (BJH) model. The photocatalytic properties were conducted in detail, and the results demonstrated outstanding photodegradation efficiency under sunlight with 98.8% MB degradation in just 27 minutes.

2. Experimental and methods

2.1. Materials

All of the chemicals and reagents utilized for the preparation of heterojunction photocatalyst were of analytical grade 99% purity, so they were not purified further. Milli-Q water (resistivity greater than 18.2 MΩ.cm) was used during the synthesis of $MgFe_2O_4$/CuO/GO nanocomposite. Magnesium nitrate $Mg(NO_3)_2.6H_2O$, copper acetate monohydrate $Cu(CH_3COO)_2.H_2O$ and iron (III) nitrate $Fe(NO_3)_3.9H_2O$ were purchased from Fluka. Poly(vinylpyrrolidone) K30 (PVP) (MW= 40000) was purchased from DIREVO Industrial Biotechnology Germany. Graphite powder, sodium hydroxide (NaOH), sodium nitrate ($NaNO_3$) and sulfuric acid (H_2SO_4) were purchased from Sigma-Aldrich. Hydrogen peroxide (H_2O_2) and glacial acetic acid (CH_3COOH) were supplied by Scharlau. Potassium permanganate ($KMnO_4$) was purchased from AppliChem.

2.2. Synthesis of graphene oxide nano-sheets

Graphene oxide nano-sheets (GO) substrate was prepared *via* a modified Hummer's method using graphite powder as a precursor [51]. Typically, 2 g of graphite powder, 1.3 g of $NaNO_3$ and 50 mL of H_2SO_4 were charged into a 1000 mL glass beaker and stirred for 20 min at 580 rpm in an ice bath with a temperature not exceeding 5°C. Thereafter, 10.5 g of $KMnO_4$ were added stepwise to the mixture while stirring for another 1h in the same conditions. Later, 95 mL of deionized water were carefully added to the mixture and the reaction beaker was subsequently moved out of the ice bath. After that, 35 mL of H_2O_2 35 wt% were poured into the mixture and stirred for another 1h. The resulting

precipitate was treated with an aqueous solution of 1M HCl followed by washing with deionized water. The obtained precipitate of GO nano-sheets was collected and dried for 24h at 70°C.

2.3. Synthesis of $MgFe_2O_4$ nanoparticles

Nano-crystalline magnesium ferrite ($MgFe_2O_4$) was synthesized *via* an auto combustion technique, following a procedure described in our previous work [25].

2.4. Synthesis of CuO nanoparticles

Copper oxide nanoparticles (CuO NPs) was prepared via chemical precipitation approach [52]. In a typical reaction apparatus, 1.199 g of $Cu(CH_3COO)_2.H_2O$ was dissolved in 300 mL of DI water and agitated with 1 mL glacial acetic acid at temperature of 60°C. Sodium hydroxide (1M; 100 mL) was gradually added to the mixture as a basifying medium to cause the precipitation of the heavy black product. The precipitate was washed sequentially with DI water and ethanol several times, and finally dried for 6h at 80°C.

2.5. Synthesis of $MgFe_2O_4$-CuO/GO nanocomposite photocatalyst

Nanocomposite photocatalyst was successfully prepared via microwave-ultrasonic procedure (see Figure 1). In a Muller furnace, equal amounts of $MgFe_2O_4$ and CuO were mixed, finely ground, and thermally treated for 2h at 400°C. The resulting $MgFe_2O_4$-CuO nanocomposite (0.5 g) was dispersed in 50 mL of DI water and added to another dispersion containing (0.3 g) GO nano-sheets and 50 mL DI water. The mixture was sonicated for 2h at 40°C, then microwaved for 10 min. Finally, the resulting $MgFe_2O_4$-CuO/GO nanocomposite was isolated, washed several times with DI water and ethanol and dried for 6h at 60°C.

2.6. Materials characterization

Structural characterization of the newly-synthesized magnetic nanocomposite photocatalyst and the starting materials was performed using Fourier-Transform Infrared Spectroscopy (FTIR) on a model Shimadzu 8400 spectrophotometer in the 400-4000 cm^{-1} range, and elemental analysis by energy-dispersive X-ray spectroscopy (EDX) (ZEISS Sigma 300). Raman spectroscopy is a well-suited technique for determination of the structural defects in the crystal structure of GO-based nanocomposites. Raman spectra of as-synthesized GO nano-sheets and MgF_2O_4-CuO@GO nanocomposite were monitored in the spectral region of 100-3600 cm^{-1}. The crystalline structures of the synthesized materials were examined by X-ray powder diffractometry (XRD) (XRD-6000 Shimadzu) using Cu Kα radiation (λ = 1.5406 Å), 10°-80° 2θ, and 5 degrees/s scan rate. The crystallite size (D) of the prepared materials was calculated from the width of the most intense peak using the Debye-Scherrer equation (Eq. 1) [53].

$$D_{XRD} = \frac{K\lambda}{\beta \cos\theta} \qquad (1)$$

where K is a constant related to the crystallite shape (K = 0.9), θ is the Bragg angle and β is the contribution of the crystallite size to the full width at half maximum (FWHM) of the corresponding diffraction peak in radians.

The lattice constant a was calculated by using the following relation (Eq. 2):

$$a = d_{hkl}\sqrt{h^2 + k^2 + l^2} \qquad (2)$$

where d the interplanar distance for the plane hkl. The degree of crystallinity (Dx) was calculated using the following formula (Eq. 3) [42]:

$$Crystallinity\ \% = \frac{Diffraction\ peak\ intensity}{Total\ intensity} \times 100 \qquad (3)$$

The crystalline phases were identified by comparison with the Joint Committee on Powder Diffraction Standards (JCPDS) database.

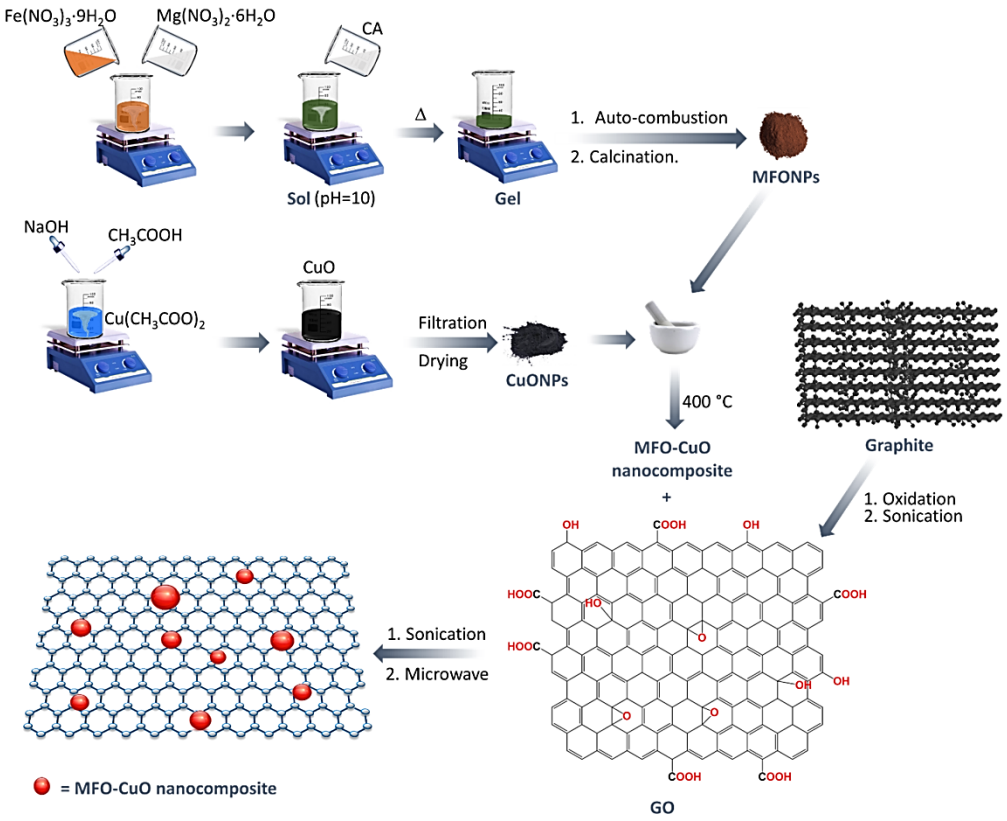

Fig. 1. Synthesis route of $MgFe_2O_4$-CuO/GO heterojunction magnetic nanophotocatalyst

Field Emission Scanning Electron Microscopy (FE-SEM) (Model: ZEISS Sigma 300) was used to scan the surface morphology of the prepared nano-photocatalyst and the starting materials. The particle size was also determined by Transmission Electron Microscopy (TEM) (JEOL, JEM-2100F, 200 kV). The Brunauer-Emmett-Teller (BET) method and Barrett-Joyner-Halenda (BJH) model were used to determine the specific surface area, pore size distribution, and pore volumes of the synthesized

materials. The optical absorption features of the nanocomposites were investigated via Diffuse Reflectance Spectroscopy (UV-vis-DRS) JASCO-V650 with an integrating sphere (ILV-724) (λ= 300-800 nm). The magnetization measurements were made under ambient conditions using a vibrating scanning magnetometer (VSM) (Cryogenic Limited PPMS) under an applied field of ±1 T.

2.7. Photocatalytic testing

The photocatalytic performance of the newly-synthesized $MgFe_2O_4$-CuO/GO magnetic nanophotocatalyst was assessed using a methylene blue batch photodegradation reaction under solar illumination. Every run was performed on a dispersion of 0.03 g of photocatalyst in 50 mL of 10 mg L^{-1} methylene blue aqueous solution in a 250 mL glass reactor. The reactor contents (i.e. photocatalyst and MB aqueous solution) were stirred in the dark for 30 min to achieve adsorption equilibrium between MB, photocatalyst and water. Thereafter, the photodegradation reaction was initiated by irradiating the reactor contents with visible light for 180 min. Photocatalytic evaluation was performed during photocatalytic process by withdrawing 5 mL of the irradiated suspension every 5 min. All the experiments were carried out under direct sunlight (measured as 100,000±100 lux), without stirring, over set periods of sunlight in the natural environment. The withdrawn samples were instantly filtered and exposed to an applied magnetic field to separate the nanocomposite from the dye solution. The samples were tested using a UV-visible spectrophotometer at λ_{max} = 664 nm to determine the concentration of methylene blue after the elapsed time interval (C_t). The following equation (Eq. 4) was used to calculate dye degradation efficiency over time.

$$\%Degradation = \frac{(C_i - C_t)}{C_i} \times 100 \qquad (4)$$

where C_i is the initial concentration of the dye and C_t the concentration at a given reaction time.

3. Results and Discussion

3.1. FTIR, XRD and Raman measurements

FTIR spectra (Fig. 2a) were used to examine the characteristic groups belonging to $MgFe_2O_4$ and CuO NPs, GO nano-sheets, $MgFe_2O_4$-CuO and the novel magnetic photocatalyst $MgFe_2O_4$-CuO/GO nanocomposite. Distinctive peaks related to the magnesium ferrite and copper oxide NPs were observed in the fingerprint region of the FTIR spectra. The FTIR spectrum of $MgFe_2O_4$ NPs revealed two prominent absorption bands at 561 and 424 cm^{-1}, which were attributed to the ionic bonds (Fe-O and Mg-O), indicating the formation of $MgFe_2O_4$ [53]. For CuO nanoparticles, broad bands located at 1436 cm^{-1} and 3429 cm^{-1} respectively were attributed to the stretching and bending vibrations of hydroxyl groups, whereas bands located in the 424-611 cm^{-1} range represented the Cu-O stretching vibrations [54]. The following distinct bands were visible in the FTIR trace for GO nano-sheets: O-H bond: 3421 cm^{-1}, C=O bond: 1718 cm^{-1}, C=C aromatic bond: 1631 cm^{-1}, C-O-C ether linkages: 1226

cm^{-1}, 1064 cm^{-1} (C-O bond) [55]. For the $MgFe_2O_4$-CuO semiconductor alloy, there was a noticeable shift in the positions of vibrational bands related to the starting materials i.e. MFO and CuO. For instance, MFO peaks normally located at 424 cm^{-1} and 561 cm^{-1} were found at 415 cm^{-1} and 574 cm^{-1}, while CuO peaks in the 424-611 cm^{-1} range were found at 601, 497 and 439 cm^{-1} with lower intensities in the $MgFe_2O_4$-CuO semiconductor alloy. These apparent shifts may be partly due to change in particle size [56],but are most likely to be due to interfacial interactions between the components in the hybrid materials. However, the featured bands observed for the GO nano-sheets were also found to be less intense upon decorating GO nano-sheets with $MgFe_2O_4$-CuO semiconductor alloy. This reduction in GO bands intensities is evidence that anchoring of the $MgFe_2O_4$-CuO upon GO nano-sheets had occurred.

The XRD patterns of the $MgFe_2O_4$-CuO/GO photocatalyst and the starting materials are shown in Fig. 2b. The XRD pattern of the prepared $MgFe_2O_4$ nanoparticles calcined at 900 $^{\circ}$C revealed sharp, intense crystalline diffraction peaks of the (111), (220), (311), (222), (400), (331), (422), (511), (440), (531), (620), and (533) crystallographic planes that respectively corresponded to 2θ values of 18.3°, 30.1°, 35.5°, 37.1°, 43.1°,49.5°, 53.4°, 57.0°, 62.6°, 64.0°, 70.9°, and 74.0°. These dominant diffraction peaks were indexed to those from the spinel magnesium ferrite (face-centred cubic phase Fd3m space group, JCPDS card no. 01-071-1232) with no peaks associated with Mg and Fe oxides. Small peaks related to lattice planes of α-Fe_2O_3 (JCPDS card no. 80-2377) were assigned as a minor second phase with MFO.

The XRD peaks of CuO NPs appeared at 2θ values of 32.50°, 35.40°, 38.60°, 45.50°, 47.40°, 53.38°, 58.16°, 62.49°, 66.16°, 67.85°, 67.88, 72.40° and 74.96° were respectively linked to *hkl* values of (110), (-111), (111), (-112), (-202), (020), (202), (-113), (022), (-311), (220), (311) and (004) crystallographic planes of the monoclinic structure (C2/c space group) of the CuO NPs (JCPDS card No. 33-0664). The diffraction peaks of the GO nano-sheets appeared at 2θ values of 10.5° and 25.5° which corresponded to the (001) and (002) planes of an ordered few-layer structure of graphene oxide [57]. The XRD pattern for the prepared $MgFe_2O_4$-CuO semiconductor alloy presented the same crystallographic planes as the starting materials MFO and CuO NPs and no effect on the lattice of $MgFe_2O_4$ NPs was observed upon CuO anchoring. The XRD pattern for the novel $MgFe_2O_4$-CuO/GO magnetic nanocomposite photocatalyst revealed crystallographic planes with multi-phases (cubic and monoclinic) correlated to the starting materials, with no shifted peaks that would indicate lattice expansion or contraction. Moreover, the obvious increase in the intensities of the diffraction peaks (400), (331), and (533) is evidence for the growth of the crystallographic planes of the prepared photocatalyst. According to the Scherrer equation, it was found that the crystallite size for (400) (331),

and (533) planes was 36.71 nm for the pristine MFO while it was 41.75 nm for MFO in MFO-CuO/GO photocatalyst. Furthermore, a clear reduction in the intensity of the CuO diffraction peaks, especially for the (020), (202), (-113), (022), (-311), (220), (311) crystallographic planes was observed for the MFO-CuO/GO nanocomposite, which might be attributable to the emergence of CuO amorphous structures [58].

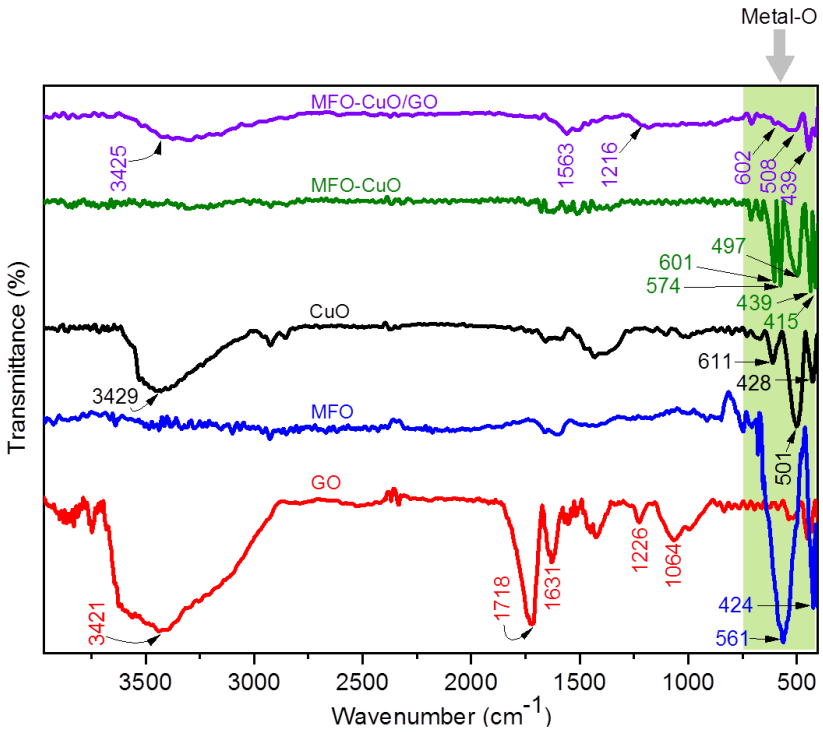

Fig. 2a: FTIR spectra of GO nano-sheets, $MgFe_2O_4$, CuO NPs and $MgFe_2O_4$/CuO/GO nanocomposite photocatalyst.

Fig. 2c shows the Raman spectra of the prepared GO nano-sheets and $MgFe_2O_4$-Cu/GO magnetic nanocomposite. The Raman trace featured two distinct bands, the diamond band and graphite band respectively denoted as D-band and G-band. The D peak at 1348 cm^{-1} and G peak at 1589 cm^{-1} were clearly observed, which was the typical sign of graphene. In the $MgFe_2O_4$-Cu/GO spectrum, small intense peaks at 216, 336, 497, 578, 676 and 726 cm^{-1} respectively belonging to F_{2g} (1), E_g, F_{2g} (2), F_{2g} (3) and A_{1g} Raman-active vibration modes of $MgFe_2O_4$-CuO. The relative intensity ratio I_D/I_G was 1.036 for GO nano-sheets, while it was 0.919 for the $MgFe_2O_4$-Cu/GO magnetic nanocomposite, indicating the presence of graphitic character. However, both D and G bands of the as-prepared $MgFe_2O_4$-Cu/GO were slightly shifted to the lower frequency region (1343 and 1582 cm^{-1}) when compared to the D and G bands of GO nano-sheets, indicating slight reduction of GO to rGO upon $MgFe_2O_4$-Cu during the microwave-ultrasonic process [27].

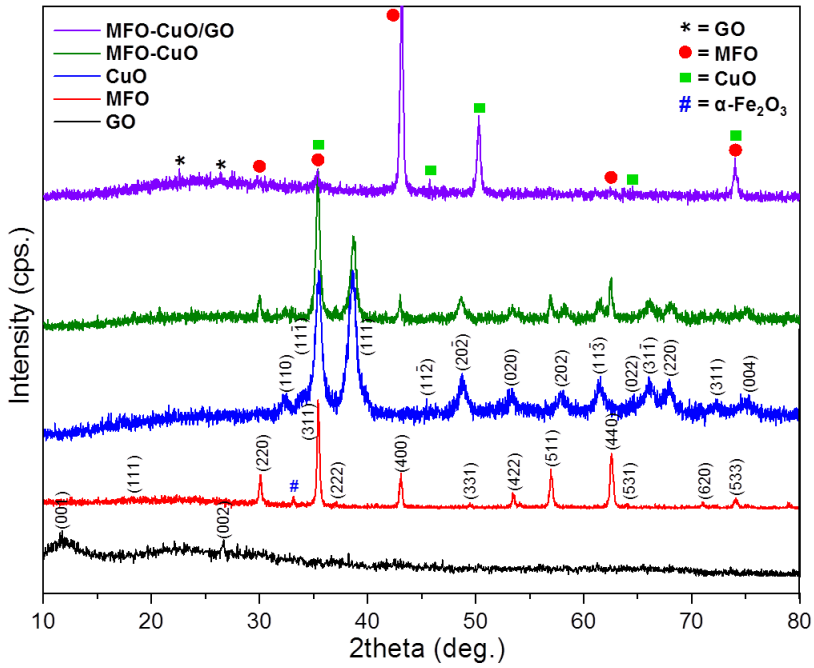

Fig. 2b: XRD patterns of GO nano-sheets, pristine $MgFe_2O_4$, CuO NPs and $MgFe_2O_4$/CuO/GO nanocomposite photocatalyst.

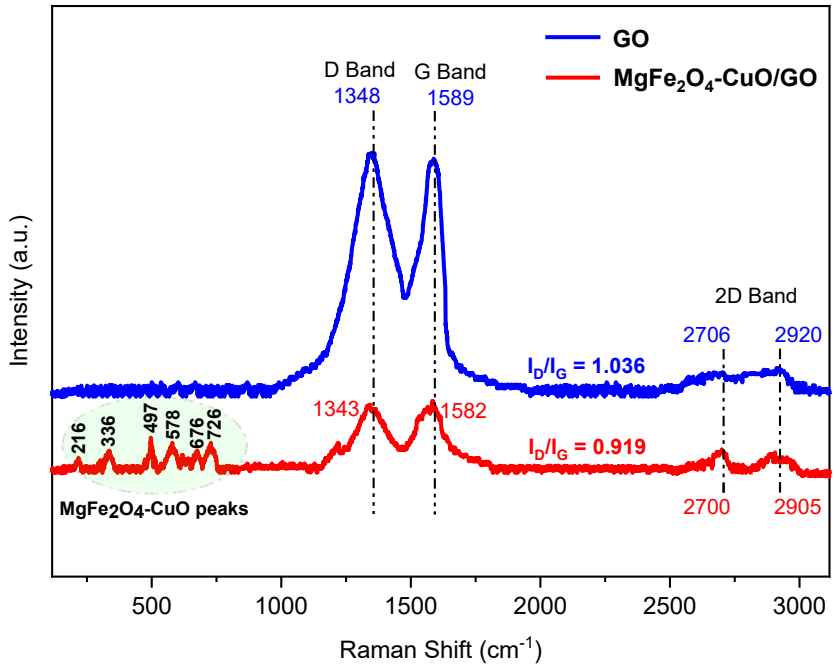

Fig. 2c: Raman spectra of GO nano-sheets and $MgFe_2O_4$/CuO/GO nanocomposite photocatalyst.

3.2. Surface studies and elemental compositions

Surface morphologies and elemental compositions of the prepared nanomaterials were obtained by FESEM, TEM, high-resolution (HR)-TEM, selected-area electron diffraction (SAED) and EDX techniques. Fig. 3a-f illustrates the SEM micrographs of the new photocatalyst as well as the starting materials. The morphology of the pristine $MgFe_2O_4$ NPs calcined at 900 °C appeared as fairly uniform spherical particles with narrow size distributions (22.45 nm average size) as seen in the SEM image (Fig. 3a), and the existence of some aggregation due to the calcination process [59, 60].

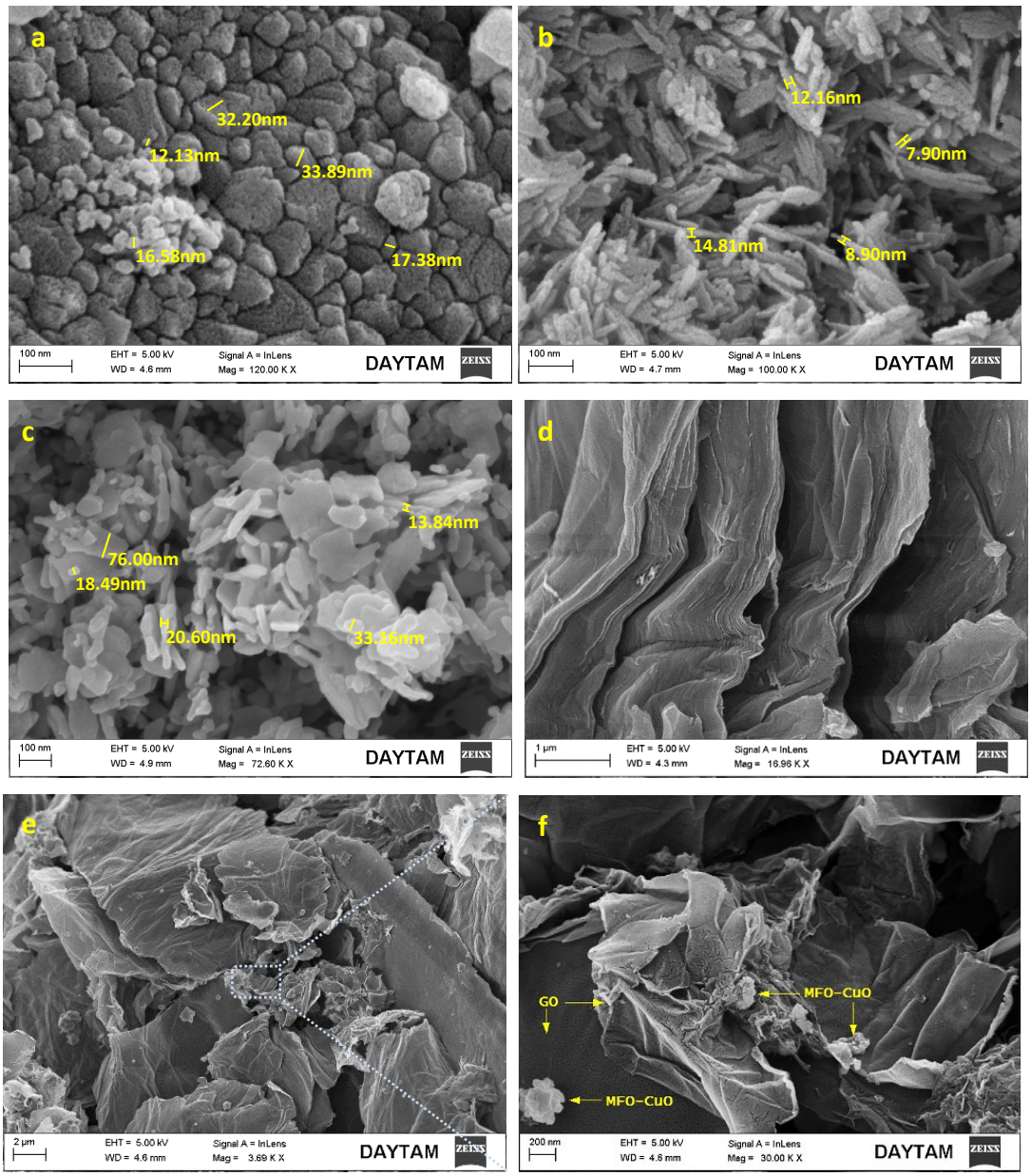

Fig. 3: SEM micrographs of a) $MgFe_2O_4$; b) CuO NPs; c) $MgFe_2O_4$-CuO NCs; d) GO nano-sheets; e, f) $MgFe_2O_4$-CuO/GO under different magnifications.

The surface morphology of the prepared CuO NPs (Fig. 3b) showed aggregates of cylindrical-like shape with a narrow size distribution and an average particle size of 10.95 nm calculated from the micrograph [61]. As can be seen in Fig. 3c, a significant change in the surface of the MFO-CuO nanocomposite was observed relative to the starting materials. The SEM image for MFO-CuO nanocomposite exhibited a high agglomeration of irregular plate-like particles with an average size of 32.4 nm. This change was caused by the interaction between the lattice planes of type Fd-3m and C2/c related to MFO and CuO NPs, respectively. The SEM micrograph (Fig. 3d) of the prepared GO presented a sheet-like morphology similar to that reported elsewhere [62, 63]. Fig. 3e,f presents SEM micrographs of MFO-CuO/GO magnetic heterojunction photocatalyst under various magnifications. Due to the high microwave energy used, it is clear to see the positively-charged MFO-CuO nanoparticles attached to the surface of GO nano-sheets via electrostatic attraction [62].

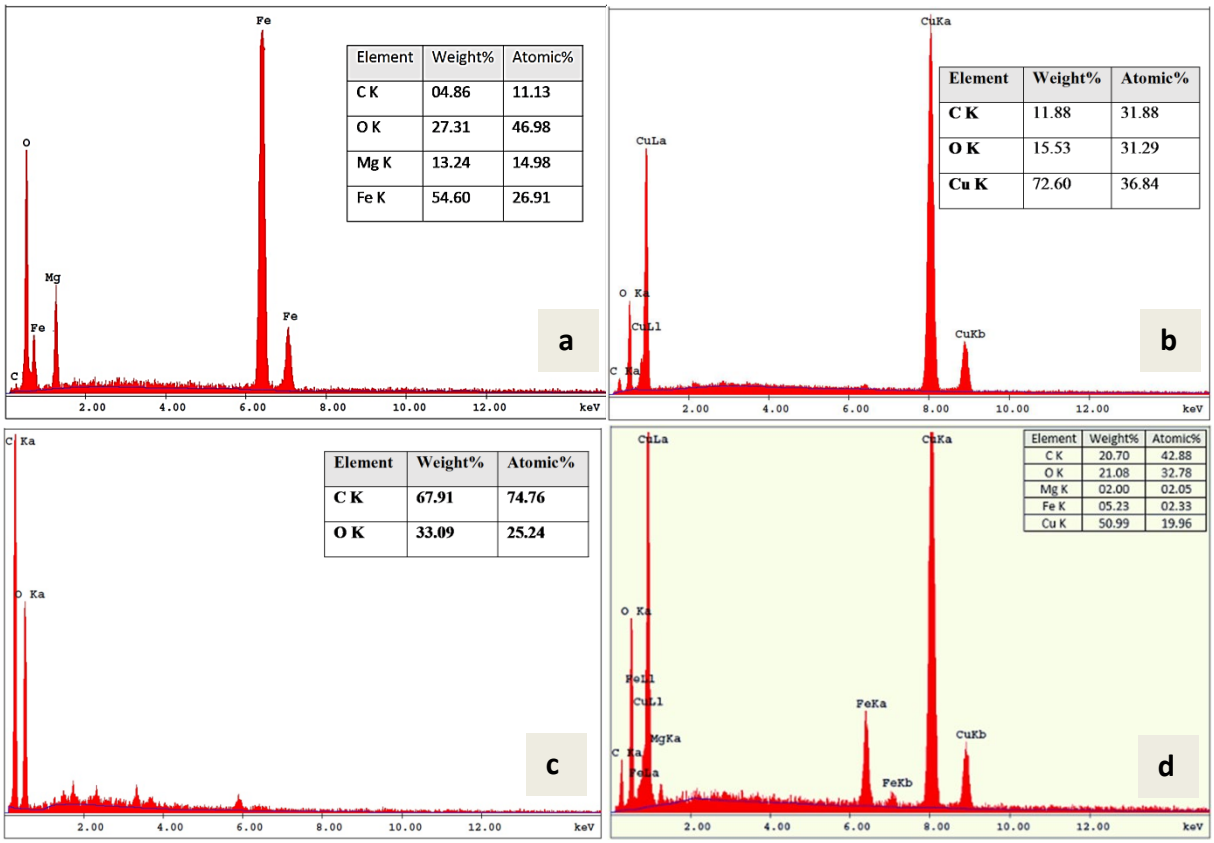

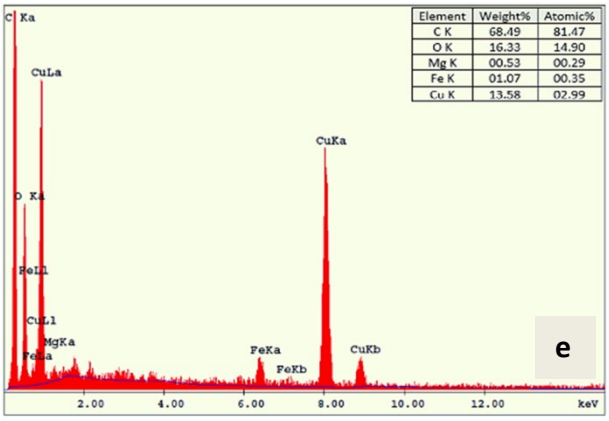

Element	Weight%	Atomic%
C K	68.49	81.47
O K	16.33	14.90
Mg K	00.53	00.29
Fe K	01.07	00.35
Cu K	13.58	02.99

Fig. 4: SEM EDX spectra of a) $MgFe_2O_4$; b) CuO NPs; c) GO nano-sheets; d) $MgFe_2O_4$-CuO NCs; e) $MgFe_2O_4$-CuO/GO NCs.

Fig. 4a-e depicts the elemental compositions and % purities measured by EDX for the individual starting materials i.e. MFO and CuO NPs, GO nano-sheets and MFO-CuO nanocomposite, as well as the prepared MFO-CuO/GO nanocomposite photocatalyst. All the EDX spectra confirmed the presence of oxygen as a result of the metal oxides content. Also, the EDX spectra (Fig. 4e) revealed a peak related to carbon atoms in the synthesized MFO-CuO/GO photocatalyst.

For further elucidation, the morphologies and crystalline structures of the neat starting materials and the synthesized photocatalyst were examined by TEM and HR-TEM with SAED patterns; the collected photographs are presented in Fig. 5a-h. The TEM image (Fig. 5a) of pure MFO NPs shows cubic and polyhedral-shaped crystals with diameters in the range 30-98 nm. The structure of MFO NPs was further validated by high-resolution (HR)-TEM (Fig. 5b), which shows lattice fringes with estimated interlayer spacings of 0.252 nm, correlated with the crystalline plane (311) belonging to MFO's XRD pattern. The polycrystalline character of MFO NPs was verified by SAED (see the inset of Fig. 5b). The pattern exhibits rings made up of bright discrete spots corresponding to multiple crystal orientations, indicating the polycrystalline nature of MFO. The TEM image for CuO NPs (Fig. 5c) shows a morphology similar to that seen in SEM (see Fig. 4b), having a high aspect ratio and a thin layer with particle size ranging from 5-29 nm. On the other hand, the HR-TEM image (Fig. 5d) of CuO NPs reveals lattice fringes with interlayer spacing values of 0.252 and 0.233 nm which, respectively correspond to crystallographic planes (-111) and (111) of CuO. Additionally, the SAED patterns of CuO NPs (see the inset of Fig. 5d) displays rings with a few discrete spots. The rings may be due to polycrystalline nanoscale CuO particles, and the spots come from better-orientated crystal planes of a monocrystalline phase.

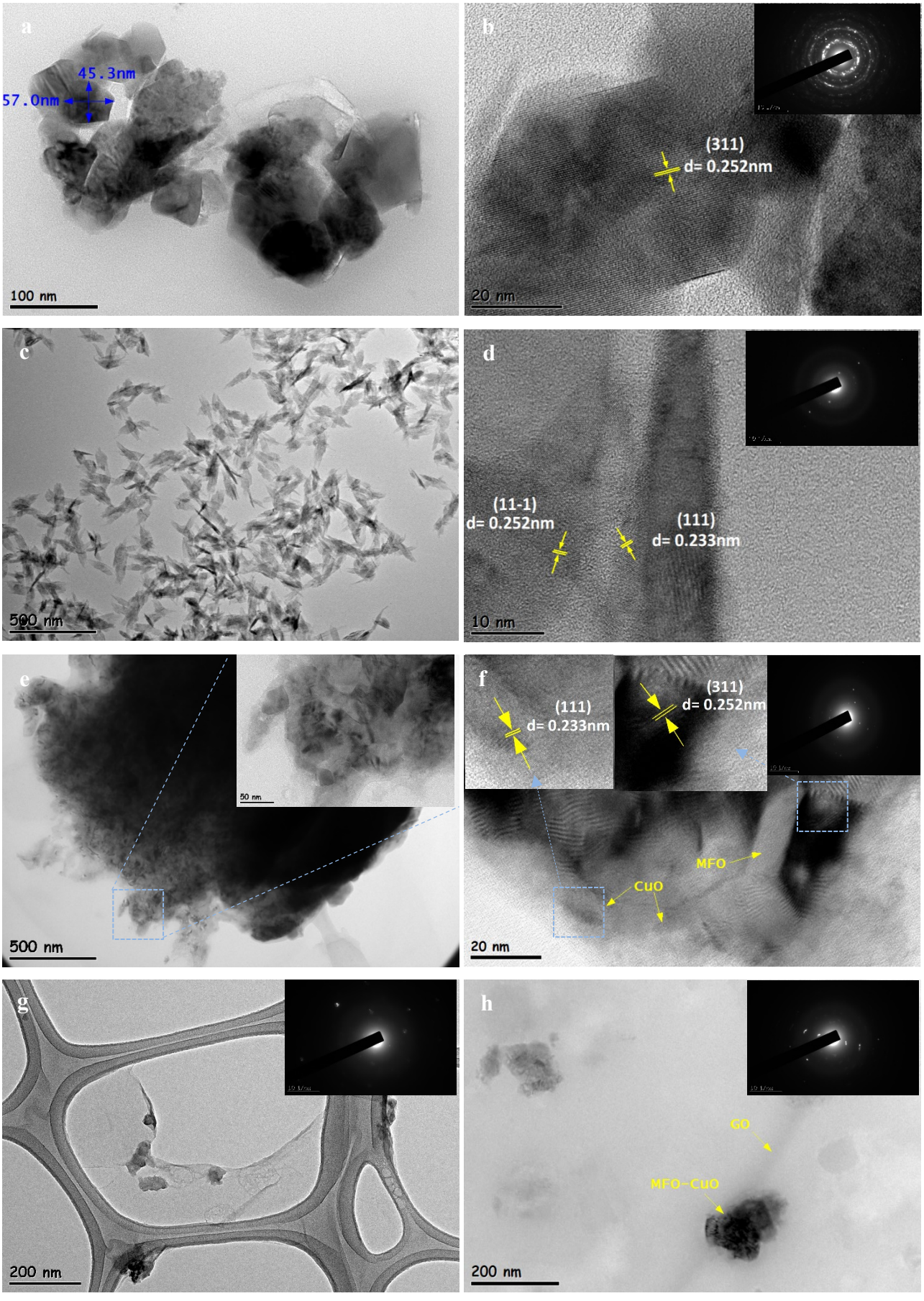
a
45.3nm
57.0nm
100 nm
b
(311)
d= 0.252nm
20 nm
c
500 nm
d
(11-1)
d= 0.252nm
(111)
d= 0.233nm
10 nm
e
50 nm
500 nm
f
(111)
d= 0.233nm
(311)
d= 0.252nm
MFO
CuO
20 nm
g
200 nm
h
GO
MFO-CuO
200 nm

Fig. 5. TEM images of a) MFO NPs, c) CuO NPs, e) MFO-CuO nanocomposite, g and h) GO nano-sheets and MFO-CuO/GO photocatalysts with their SAED patterns; (HR)-TEM images and SAED patterns of MFO NPs, CuO NPs, and MFO-CuO nanocomposite labelled b, d, and f, respectively.

The morphology of the produced MFO-CuO semiconductor alloy (see Fig. 5e and the inset of Fig. 5e) clearly shows large numbers of MFO NPs surrounding CuO NPs, forming larger aggregates. This could indicate that high aspect-ratio CuO NPs are covered with low aspect-ratio MFO NPs. Furthermore, a few random spots appeared in the SAED pattern (see the inset of Fig. 5f), illustrating that combining high diffraction MFO NPs with low diffraction CuO NPs reduces the crystallinity of the produced MFO-CuO semiconductor alloy. The number of active sites of MFO-CuO crystals will surely decrease in the presence of such aggregation, which will impact the heterogeneous activation process [64].

The HR-TEM image of the prepared MFO-CuO alloy (see Fig. 5f and the inset of Fig. 5f) displays the lattice fringes with interlayer spacing values of 0.252 (311) nm and 0.233 nm (111), which respectively correspond to MFO and CuO NPs in the MFO-CuO alloy. The TEM observations for the prepared GO nano-sheets (Fig. 5g) reveal a thin layer including some sinuous structures with relatively smooth surfaces. Additionally, the SAED patterns of the prepared GO nano-sheets (see the inset of Fig. 5g) did not display conspicuous rings despite the existence of certain diffraction spots, indicating that the GO retained crystalline order. Fig. 5h is a TEM image of the MFO-CuO/GO nanocomposite photocatalyst. It can be seen that MFO-CuO semiconductor hybrid is partially anchored on the GO nano-sheets. This partial anchoring may improve access to the active sites, resulting in higher photocatalytic efficiency. Moreover, the SAED patterns of the photocatalyst (Fig. 5h inset) indicates low crystallinity, while keeping the diffraction signatures of the starting materials. All the foregoing properties support the incorporation of the MFO-CuO alloy onto GO nano-sheets and hence, we have engineered a novel heterojunction photocatalyst made up of metal oxides and a carbon-based nanomaterial that may prove to circumvent some of the limitations of other photocatalysts.

3.3. N_2 adsorption-desorption analysis

Fig. 6a-h shows the N_2 adsorption-desorption isotherms and pore size distribution curves of the prepared nanomaterials. All the prepared nanomaterials revealed type IV isotherms according to the IUPAC classification. The isotherms also show H3-type hysteresis loops at relatively high P/P^o (0.30-0.95), indicating the existence of mesoporosity in the studied samples. This sort of loop, however, is indicative of agglomerates of plate-shaped particles that generate slit-shaped pores [65]. The disappearance of a hysteresis loop for MFO in MFO-CuO sample (see Fig. 6e) may be due to the blocking of MFO pores by CuO deposition. The specific surface area S_{BET} for the studied

nanomaterials was calculated from the N_2 adsorption-desorption branch according to the multipoint BET method, and the pore volume and pore size were calculated from the nitrogen desorption branch based on the Barrett-Joyner-Halenda (BJH) model. According to the data presented in Table 1, the obtained S_{BET} values were 1.463, 58.8, 31.94, 8.25, and 96.12 $m^2.g^{-1}$, respectively for $MgFe_2O_4$ NPs, CuO NPs, GO nano-sheets, $MgFe_2O_4$-CuO nanocomposite and $MgFe_2O_4$-CuO/GO nano-catalyst. The results showed that the new $MgFe_2O_4$-CuO/GO photocatalyst had a higher specific surface area (96.12 $m^2.g^{-1}$) than $MgFe_2O_4$-CuO nanocomposite and GO nano-sheets, indicating efficient distribution of $MgFe_2O_4$-CuO on the GO surface. The nanocatalyst displayed narrow-range mesoporous domains extending from 2.1 to 27 nm, with an effective pore size of 2.9 nm and pore volume of 0.0521 $cm^3.g^{-1}$. Combining different nanoparticles ($MgFe_2O_4$, CuO and GO) of different porosities, crystallinities, and mineral phases, which are the main factors influencing the specific surface area SSA of nanomaterials, could explain why the $MgFe_2O_4$-CuO/GO nanocatalyst had greater SSA than pristine $MgFe_2O_4$, despite the increase in the particle size on the incorporation of CuO and GO. In addition, the gentle heating makes the nano-crystals slightly larger but more well-defined, so the active surfaces are more easily available.

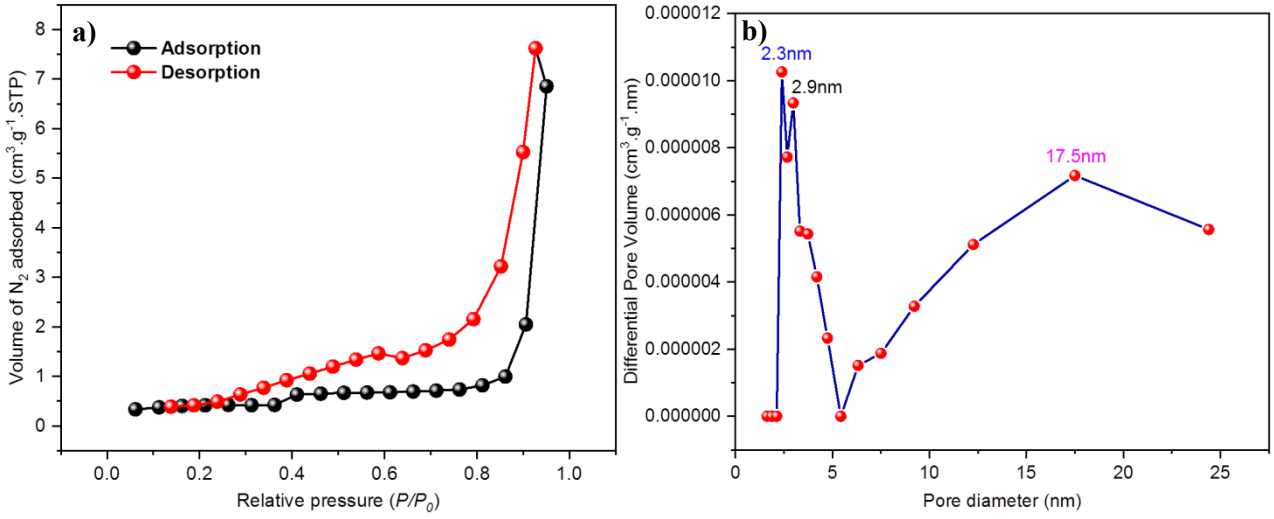

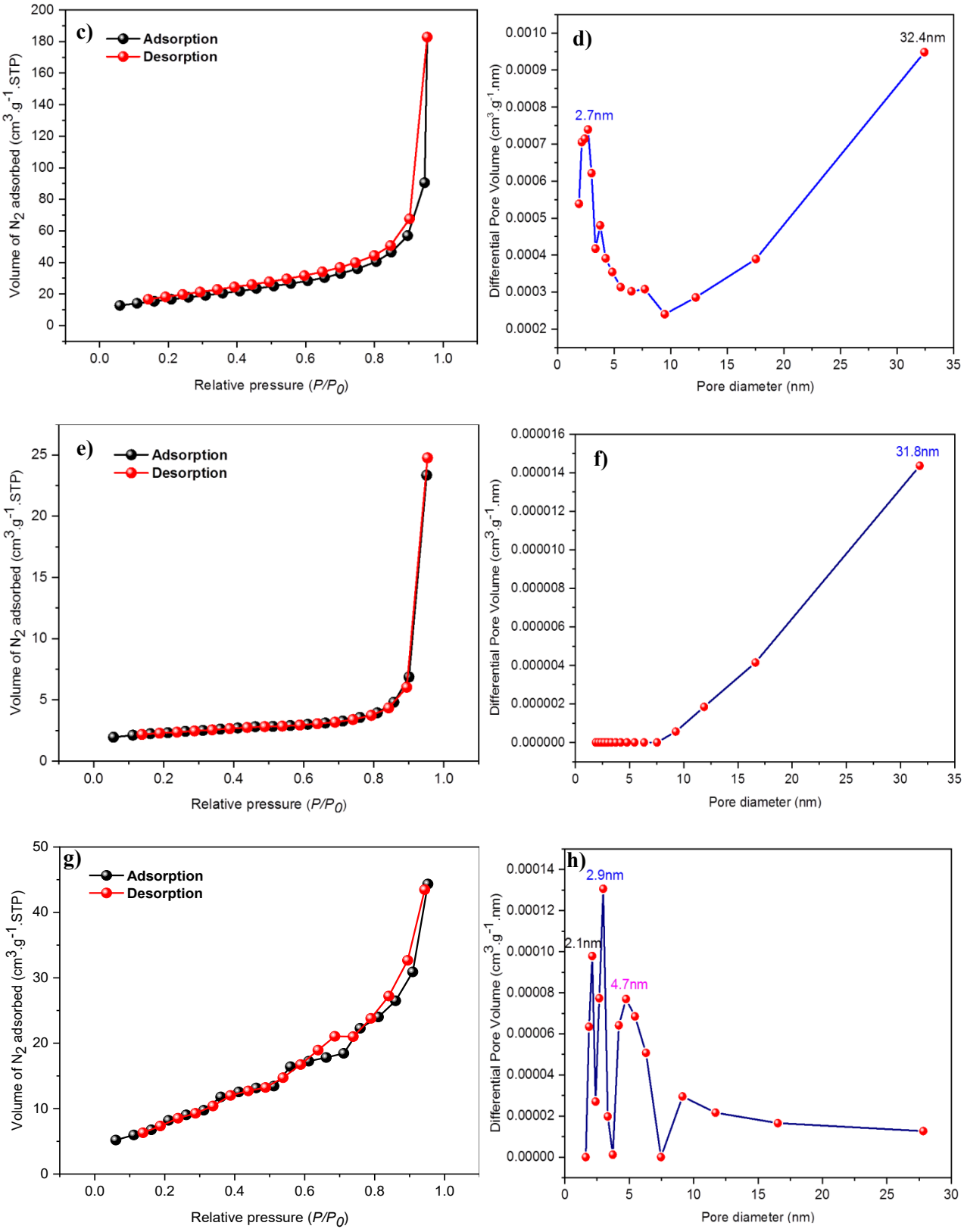

Fig. 6. N_2 adsorption-desorption isotherms: (a) $MgFe_2O_4$ NPs, (c) CuO NPs, (e) $MgFe_2O_4$-CuO NCs and (g) $MgFe_2O_4$-CuO/GO photocatalyst, with their BET surface area and pore size distribution plots labelled (b), (d), (f), and (h), respectively.

3.4. Magnetic study

One of the most valuable characteristics of magnetic photocatalysts is their strong magnetism. In certain chemical and/or petrochemical industries, this can be used to separate the catalyst swiftly from an aqueous mixture. Therefore, in this work, the magnetic features of the prepared $MgFe_2O_4$ NPs, $MgFe_2O_4$-CuO NCs, and $MgFe_2O_4$-CuO/GO nanocatalyst were evaluated with a vibrating sample magnetometer (VSM) at room temperature. The magnetic hysteresis loops of the studied nanomaterials are shown in Fig. 7a,b and the obtained magnetic parameters are listed in Table 1. The magnetization curves reveal that all MFO, MFO-CuO and MFO-CuO/GO are soft superparamagnetic nanomaterials having minimal remanence M_r and coercivity Hc, with saturation magnetization Ms values of 28.91 $emu.g^{-1}$, 18.11 $emu.g^{-1}$, and 16.72 $emu.g^{-1}$, respectively. The low Ms value for MFO-CuO semiconductor alloy in comparison with MFO NPs could be due to a dilution effect. $MgFe_2O_4$ NPs would have two Fe(III) ions, and hence 10 unpaired electrons, per formula unit, hereas CuO NPs should have 1 unpaired electron and graphene oxide have none (diamagnetic). So MFO is much more strongly magnetic than CuO or GO, and when they are combined together, the saturation magnetization should be lower. The decrease in the saturation magnetization of the MFO-CuO/GO nanocatalyst may be due to the diamagnetic nature of GO nano-sheets in the nanocomposite and/or to the presence of a magnetically dead or antiferromagnetic layer on the nanocomposite surface [66]. Although the existence of such a non-magnetic region on the catalyst surface reduces its apparent magnetic moment, it has been reported that a saturation magnetization of 16.3 $emu.g^{-1}$ is sufficient for magnetic separation [67], so our novel photocatalyst with saturation magnetization (16.72 $emu.g^{-1}$) is sufficient for magnetic separation from an aqueous mixture when an external magnetic field is applied.

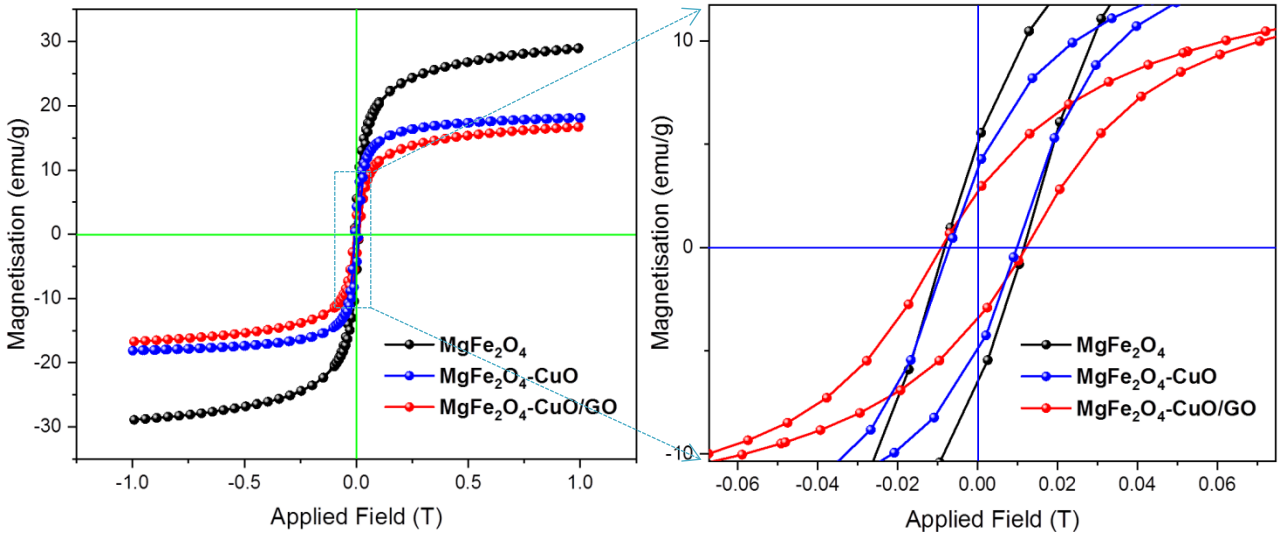

Fig. 7. Magnetic hysteresis curves of the studied nanomaterials at room temperature.

Table 1. Physical parameters of the studied nanomaterials.

Parameters	GO	$MgFe_2O_4$	CuO	MFO-CuO	MFO-CuO/GO
Crystallite size (D_{SEM}) nm	-	22.45	10.9	32.4	-
Crystallite size (D_{TEM}) nm	-	30-98	5-29	-	-
Crystallite size (D_{XRD}) nm	-	36.696	11.105	27.807	41.75
Crystallinity (%)	-	82.87	69.60	60.47	51.45
Specific surface area (S_{BET}) $m^2.g^{-1}$	31.94	1.463	58.83	8.258	96.12
Pore volume, (V_p) $cm^3.g^{-1}$	0.0738	0.0134	0.282	0.0378	0.0521
Pore diameter (D_p) nm	22.98	2.40	32.42	31.77	2.90
Saturation magnetization, (M_S) emu. g^{-1}	-	28.91	-	18.11	16.72
Remanence (M_R) emu. g^{-1}	-	5.548	-	2.97	4.44
Coercive field (H_C) Oe	-	117	-	97	121.9
Bandgap energy (eV)	3.3	1.87	1.99	1.76	1.69

3.5. Optical bandgap analysis

Nanomaterials with photocatalytic characteristics and a low optical bandgap energy can easily collect photons in the visible light range. UV-visible diffuse reflectance (DRS) spectroscopy was used to assess the optical bandgap energy of as-prepared MFO NPs, CuO NPs, GO nano-sheets, MFO-CuO nanocomposite and MFO-CuO/GO nanocatalyst. Tauc's equation was utilized to calculate the optical bandgap energy (Eg) of the studied samples [68].

$$(\alpha h\nu)^n = A(h\nu - Eg) \qquad (5)$$

where α is the absorption coefficient, h is Planck's constant, ν is the photon frequency, Eg is the optical bandgap energy, A is a constant and n has a value of 2 for a direct bandgap and ½ for an indirect bandgap [54].

The DRS spectra (see Fig. 8a), reveals absorbance features at 385, 365, 383, 289 and (291 & 388) nm, respectively attributed to MFO NPs, CuO NPs, MFO-CuO NCs, GO nano-sheets and MFO-CuO/GO nano-catalyst. The DRS spectra for our nanocatalyst was red-shifted as compared to the starting materials, essentially extending the light response range into the visible region. This implies that the optical characteristics of our nanocatalyst have improved in the visible light area. Plotting $(\alpha h\nu)^2$ versus $h\nu$ (Fig. 8b) and extrapolating the tangent line intercept with the $h\nu$ axis gives the direct bandgap energy values of 1.87, 1.99, 1.76, 3.30 and 1.69 eV, respectively corresponding to MFO NPs, CuO NPs, MFO-CuO NCs, GO nano-sheets and MFO-CuO/GO nanocatalyst. The prepared MFO-CuO NCs possess a bandgap energy of 1.76 eV, which is smaller than those of the individual metal oxides MFO and CuO, whereas MFO-CuO NCs decorated graphene oxide exhibited a bandgap energy of 1.69 eV, which is lower than those of the starting materials. The bandgaps for the individual $MgFe_2O_4$ and CuO nanoparticles are larger than the corresponding bulk values, due to the quantum size effects that are observed in small particles. When the nanoparticles are combined or anchored onto the surface of GO sheets, their effective particle size increases, so the quantum effect is less, and the bandgap becomes smaller. The bandgap of GO itself is not relevant because most of the corresponding C-C bonds would

not be directly affected by the coordination of nanoparticles to COOH groups on the GO sheets. However, this reduction in the bandgap energy may cause the emergence of new active heterojunctions between valence and conduction bands, thus producing a new electronic state in the $MgFe_2O_4$-CuO/GO nano-photocatalyst. In comparison to the individual nanomaterials under investigation, $MgFe_2O_4$-CuO/GO nanocatalyst with this new electronic state is more favourable for photocatalytic activity [69,70].

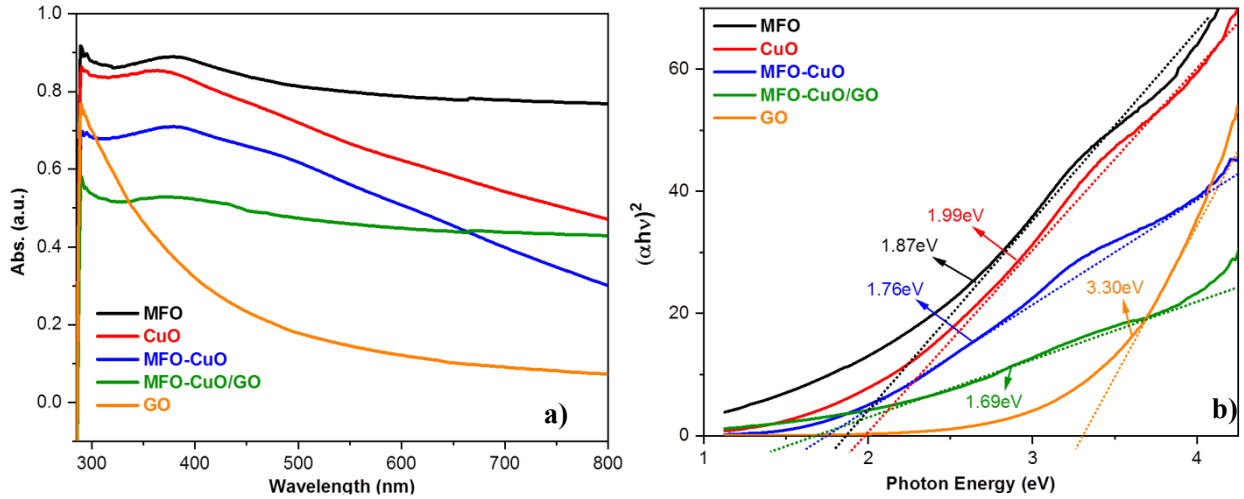

Fig. 8. (a): UV-visible diffuse reflectance spectra of the prepared nanomaterials; (b): Tauc plots

3.6. Photocatalytic activity of MFO-CuO/GO nanocatalyst

The photocatalytic performance of the $MgFe_2O_4$-CuO/GO nanocomposite was evaluated via a batch photodegradation reaction of methylene blue (MB) in aqueous solution under direct sunlight. UV-visible absorbance spectroscopy was used to determine the remaining concentration of MB after the elapsed time intervals (see Fig. 9a-f). The photocatalytic efficiencies of $MgFe_2O_4$ NPs and $MgFe_2O_4$-CuO semiconductor alloy were also investigated for comparison purposes. To examine the self-degradation of MB, an MB aqueous solution was exposed to direct sunlight for 180 min without photocatalyst, and the UV-visible results revealed that MB was sunlight-stable.

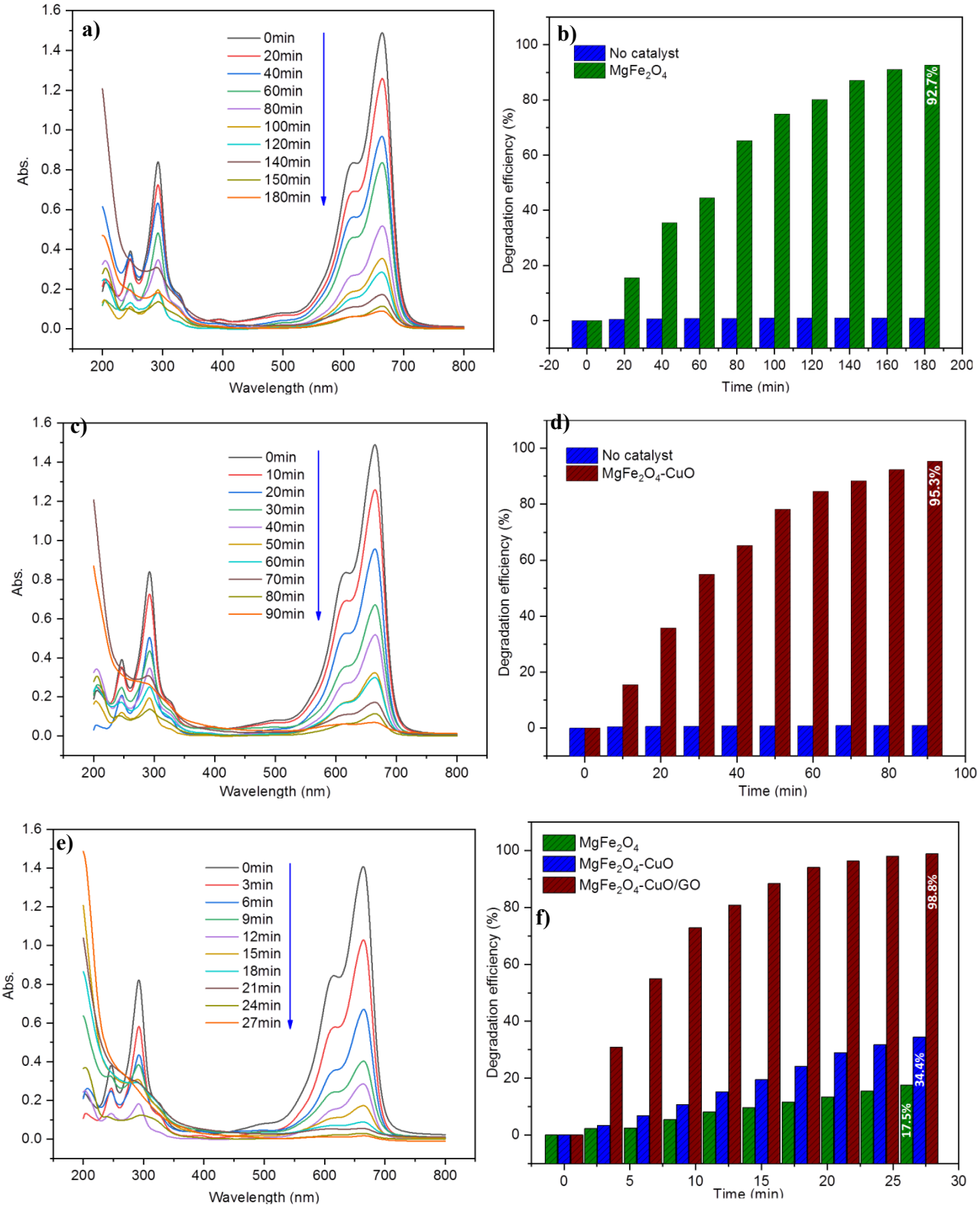

Fig. 9. Absorption spectra of MB solution after elapsed time periods in the presence of (a) $MgFe_2O_4$ NPs, (c) $MgFe_2O_4$-CuO semiconductor alloy, (e) $MgFe_2O_4$-CuO/GO nano-catalyst; (b), (d), (f) show their respective photodegradation efficiencies versus time of sunlight exposure.

It is obvious from Fig. 9a-d that the pristine $MgFe_2O_4$ NPs and $MgFe_2O_4$-CuO semiconductor alloy exhibited photodegradation efficiencies of 92.7 and 95.3% after 180 and 90 min of sunlight exposure, respectively. However, the novel $MgFe_2O_4$-CuO/GO photocatalyst showed a notable increase up to 98.8% photodegradation efficiency (Fig. 9e,f) after only 27 min of sunlight exposure. The adhesion of the $MgFe_2O_4$-CuO semiconductor alloy to 2D GO nano-sheet *via* the large specific area and extended π-π conjugation would help to prevent aggregation and would provide excellent access of the dye to the photoactive material. Thus, dramatically improving the photocatalytic activity toward MB degradation, which was attributed to the fast separation of charge carriers across the $MgFe_2O_4$-CuO@GO heterojunction. The electrical insulating property of (un-reduced) GO may also be helpful, because it provides an inert matrix that does not create a short-circuit between the p- and n-type regions. Hence the separated charges can be efficiently used for catalytic purposes [71].

3.7. Kinetic studies

The kinetics of the photo-decomposition of MB dye *via* the photocatalytic reaction over as-synthesized $MgFe_2O_4$-CuO/GO as well as $MgFe_2O_4$ NPs and $MgFe_2O_4$-CuO NCs was studied by calculating the decomposition rate constant with a pseudo-first order rate equation (Eq. 6) [72, 73].

$$\ln (C_i/C_t) = k\,t \qquad (6)$$

where k is the rate constant of the photodegradation reaction measured in (min^{-1}), t is the irradiation time in minutes, C_i is the initial concentration of MB pollutant and C_t is the concentration after the elapsed time intervals. Plotting (C_t/C_i) and $\ln(C_i/C_t)$ against the time of irradiation was respectively used to track the progress of the photocatalytic reaction and to calculate the pseudo first-order rate constant. The results shown in Fig.10a-f indicate that $MgFe_2O_4$-CuO/GO nanocatalyst has a rate constant value of 0.1668 min^{-1}, hence photodegrading the MB dye an order of magnitude faster in comparison to $MgFe_2O_4$ NPs and $MgFe_2O_4$-CuO NCs, which have rate constant values of 0.01641 and 0.00719 min^{-1}, respectively. It is also observed that the regression value R^2 is very close to unity (> 0.99) for all the tested materials. As a result, it may be inferred that the experimental data well fitted with a pseudo-first order model. The superior photocatalytic efficiency of our $MgFe_2O_4$-CuO/GO nanocatalyst may be attributed to its ability to create superoxide and hydroxyl radicals, which are responsible for the degradation process. The presence of GO nano-sheets which provide large surface area, as well as the effective separation of photo-induced electron-hole pairs and the formation of heterojunctions at the interfaces render MFO-CuO/GO nanocomposite a more efficient photocatalyst.

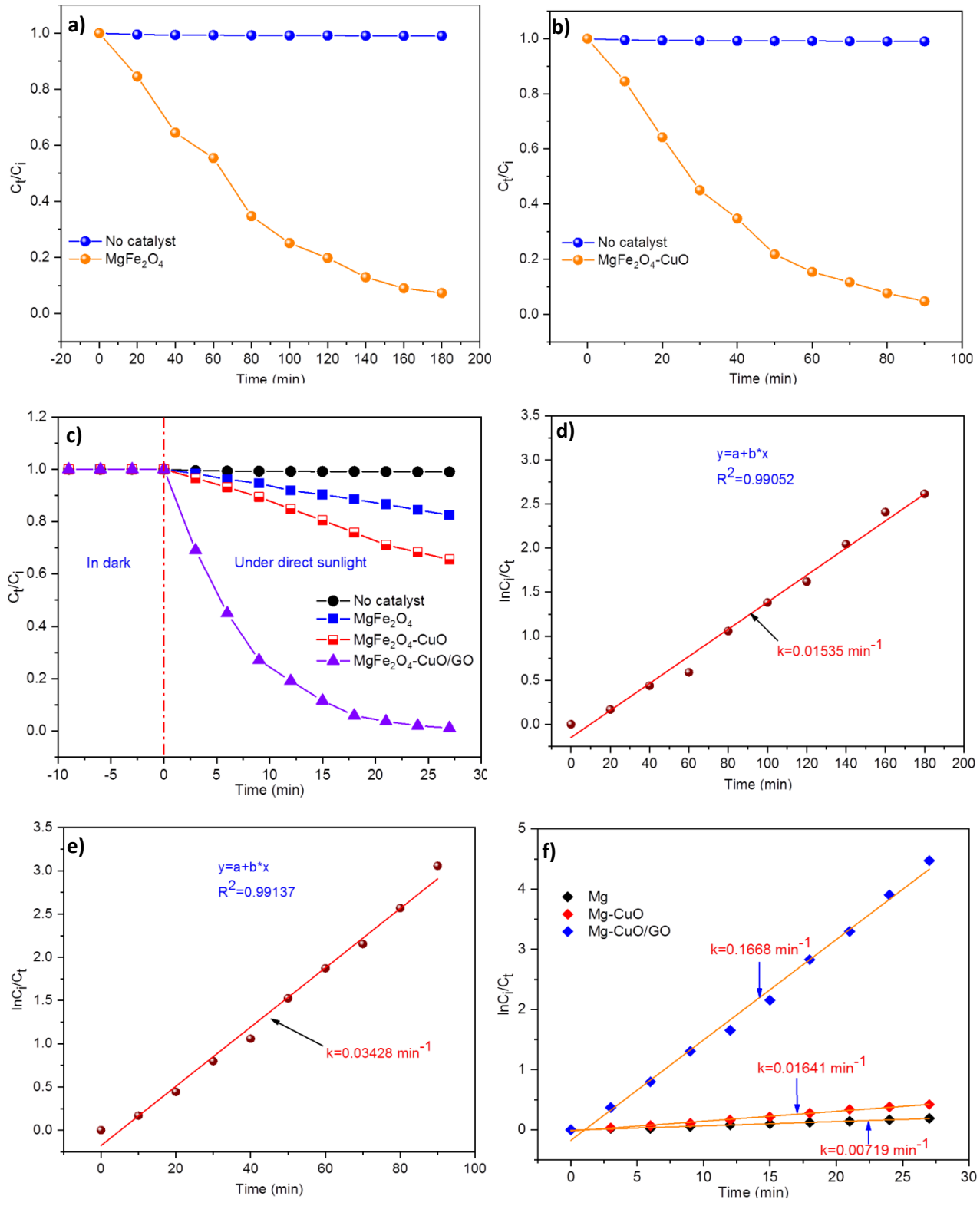

Fig. 10. Reaction kinetics plots of MB degradation over a) $MgFe_2O_4$ b) MFO-CuO c) MFO-CuO/GO, and their rate constant regression curves, respectively labelled (d-f).

3.7. Mechanism of MB photodegradation over MFO-CuO/GO nanocatalyst

The photocatalytic reaction on a photocatalyst consists of at least five major steps: i) light absorption by the photocatalyst, ii) production of photogenerated electron-hole pairs, iii) migration and recombination of the photogenerated electron-hole pairs, iv) adsorption of reactants and occurrence of redox reactions on the photocatalyst surface, v) desorption of products. In photocatalytic reactions, the photogenerated electron-hole pairs can either travel to the photocatalyst surface and initiate redox reactions, or they can recombine and generate waste heat (i.e. electron-hole pair recombination is detrimental) [71]. However, the efficient electron-hole separation in the newly-synthesized $MgFe_2O_4$-CuO/GO nanocatalyst can be further understood by calculating the conduction band (CB) and valence band (VB) edge positions of the individual $MgFe_2O_4$ and CuO NPs. The following empirical equations were utilized to determine the potentials of the VB and CB [74].

$$E_{CB} = X - E^e - 0.5E_g \qquad (7)$$

$$E_{VB} = E_{CB} + E_g \qquad (8)$$

where E_{VB} and E_{CB} are respectively the VB and CB potentials, E^e is the energy of free electrons vs. the hydrogen scale (4.5 eV), and X is the electronegativity of the semiconductor compound, which is calculated using the following equation:

$$X = [x(A)^a x(B)^b x(C)^c]^{1/(a+b+c)} \qquad (9)$$

where a, b and c are the numbers of atoms in the semiconductor compounds. Using the above formulas, the (CB) and (VB) potentials of $MgFe_2O_4$ were calculated to be 0.175 and 2.105 eV/NHE, while the (CB) and (VB) potentials of CuO NPs were 0.315 and 2.305 eV/NHE, respectively.

It is well reported that $^{\bullet}O_2^-$ and $^{\bullet}OH$ radicals are the reactive species responsible for the initiating photo-oxidative degradation reaction of MB in the catalytic system [1,25,75]. Based on that, a possible mechanism (Fig. 11) has been postulated to explain the photocatalytic activity of the $MgFe_2O_4$-CuO/GO nanocomposite. When photons of sunlight strike the MFO-CuO/GO photocatalyst, electrons (e^-) are excited from the filled valence band to the empty conduction band of MFO leaving holes (h^+) in the valence band; thus photogenerated electron-hole pairs are produced. The holes in the VB of MFO can oxidize OH^- ions to give $^{\bullet}OH$ radicals because the VB potential of OH^- is higher than the redox potential of $OH^-/^{\bullet}OH$ (1.89 eV vs. NHE) [76]. On the other hand, electrons in the CB of $MgFe_2O_4$ are unable to induce the generation of $^{\bullet}O_2^-$ radicals because of the lack of energy required to reduce ambient O_2 to $^{\bullet}O_2^-$, i.e. the CB edge position of $MgFe_2O_4$ is more positive than the redox potential of $O_2/^{\bullet}O_2^-$ (-0.33 eV vs. NHE) [71]. Incorporation of CuO nanoparticles within the nanocatalyst can result in band realignments and therefore reduce electron-hole recombination. Fig.

11 shows that both the (CB) and (VB) levels of MFO are higher than the corresponding levels of CuO NPs. Thus, during light irradiation, photogenerated electrons will migrate to the CB level of CuO, whereas photogenerated holes will travel to the VB level of MFO, resulting in spatial separation of the electron-hole pairs. When $MgFe_2O_4$-CuO is incorporated into GO nano-sheet by the microwave-assisted route, a reduction of graphitic carbon occurs from sp^3 to sp^2 hybridization which means the GO is locally reduced to rGO. The rGO is an excellent acceptor and transporter with a low Fermi level compared to that of $MgFe_2O_4$ and CuO NPs. This unique electrical properties of the new MFO-CuO/GO nanocomposite allow the electron transport from the CB level of CuO to the surface of GO nano-sheets, further enhancing the electron-hole separation. Moreover, the redox potential of graphene/graphene$^-$ (-0.08 V vs SHE) is lower than the photocatalyst CB potential, enabling fast electron migration from the photocatalyst to the GO sheet [77]. Subsequently, the electrons on the graphene surface can react with dissolved molecular oxygen releasing superoxide radicals ($^{\bullet}O_2^-$) which act as an MB oxidizer [78,79]. The photocatalytic mechanisms involved in MB degradation are outlined below:

$$MgFe_2O_4 \xrightarrow{h\nu} MgFe_2O_4\ (h_{VB}^+ + e_{CB}^-)$$

$$CuO \xrightarrow{h\nu} CuO(h_{VB}^+ + e_{CB}^-)$$

$$MgFe_2O_4(e_{CB}^-) + CuO \rightarrow MgFe_2O_4 + CuO(e_{CB}^-)$$

$$CuO(e_{CB}^-) + GO \rightarrow GO(e^-) + CuO$$

$$CuO(h_{VB}^+) + MgFe_2O_4 \rightarrow MgFe_2O_4(h_{VB}^+) + CuO$$

$$GO(e^-) + O_2 \rightarrow GO + {}^{\cdot}O_2^-$$

$${}^{\cdot}O_2^- + H_2O \rightarrow {}^{\cdot}OOH + OH^- \rightarrow H_2O_2$$

$${}^{\cdot}O_2^- + H_2O_2 \rightarrow OH^- + OH^{\bullet}$$

$$MgFe_2O_4(h_{VB}^+) + OH^- \rightarrow MgFe_2O_4 + OH^{\bullet}$$

$${}^{\cdot}O_2^- + OH^{\bullet} + MB \rightarrow \text{degradation products}$$

The formation of highly reactive and non-selective reagent hydroxyl radicals ($OH^{\bullet}$) by the catalytic breakdown of hydrogen peroxide (H_2O_2) is encourages the destruction and degradation of non-biodegradable MB dye in aqueous solution, resulting in carbon dioxide, water, and other chemicals.

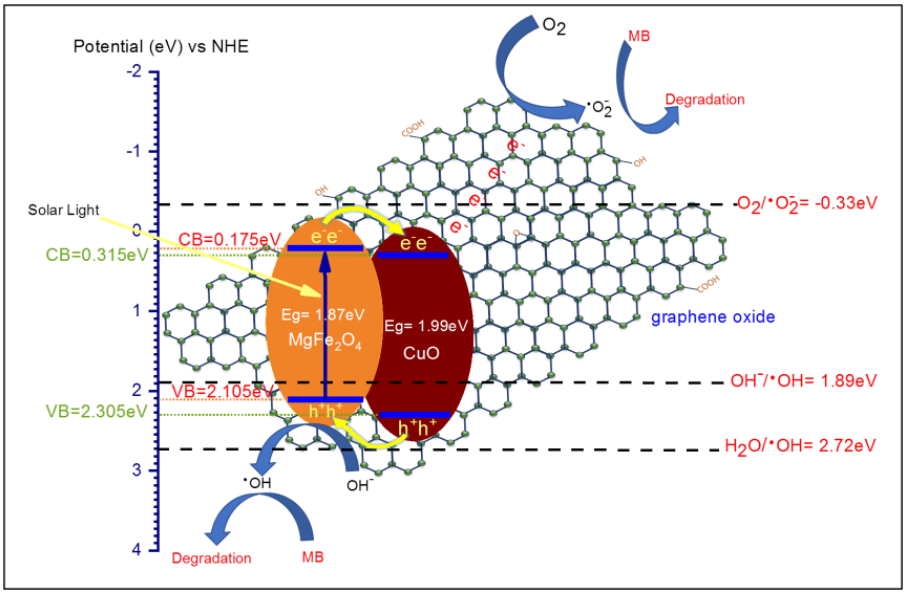

Fig. 11. Plausible mechanism of MB photodegradation over $MgFe_2O_4$/CuO/GO heterojunction magnetic photocatalyst under sunlight irradiation.

3.8. MB photodegradation performance over MFO-CuO/GO nano-catalyst

The effects of parameters such as catalyst dose, pH at which MB photodegradation occurred, and MB concentration were examined to improve the photocatalytic degradation efficiency of the new nanocatalyst. Fig. 12a shows the effect of pH on the degradation efficiency of MB over MFO-CuO/GO. Aqueous solutions of 0.1 M HCl and 0.1 M NaOH were used to maintain the pH of the dye solution. The graphical data demonstrate that the nanocatalyst had weak photocatalytic activity under acidic conditions (pH=2-4), whereas the MB dye degradation efficiency improved dramatically under mild alkaline conditions (pH=6-8). However, due to the amphoteric characteristics of our photocatalyst, the adsorption of H_2O molecules and dissociation of OH^- groups at metal surface are responsible for the production of metal hydroxyl groups (M-OH) [80]. Consequently, the photocatalyst obtains a net positive charge at acidic pH values, which prevents the cationic MB dye from adsorbing on its surface and slows down photodegradation. The strongest adsorption between the cationic MB dye and the net negatively charged photocatalyst occurs under alkaline conditions. The amphoteric features of metal hydroxides under acidic and alkaline conditions are represented as follows:

$$M\text{-}OH + H^+ \longrightarrow M\text{-}OH\text{-}H^+ \longrightarrow M\text{-}H_2O^+$$

$$M\text{-}OH + OH^- \longrightarrow M\text{-}O^- + H_2O$$

Fig. 12b depicts the effect of different doses of MFO-CuO/GO magnetic nanocatalyst on MB photodegradation. 0.03 g/L nanocatalyst was the optimum concentration for photocatalytic degradation of around 98.8 percent of MB after 27 min of sunlight exposure. Higher catalyst dose increases the number of photons absorbed by the catalyst surface, resulting in higher concentrations of

electron-hole pairs and adsorbed radicals. However, a dosage above 0.035 g/L was shown to favour photocatalyst particle aggregation, thus diminishing photon penetration into the active sites and reducing photodegradation efficiency.

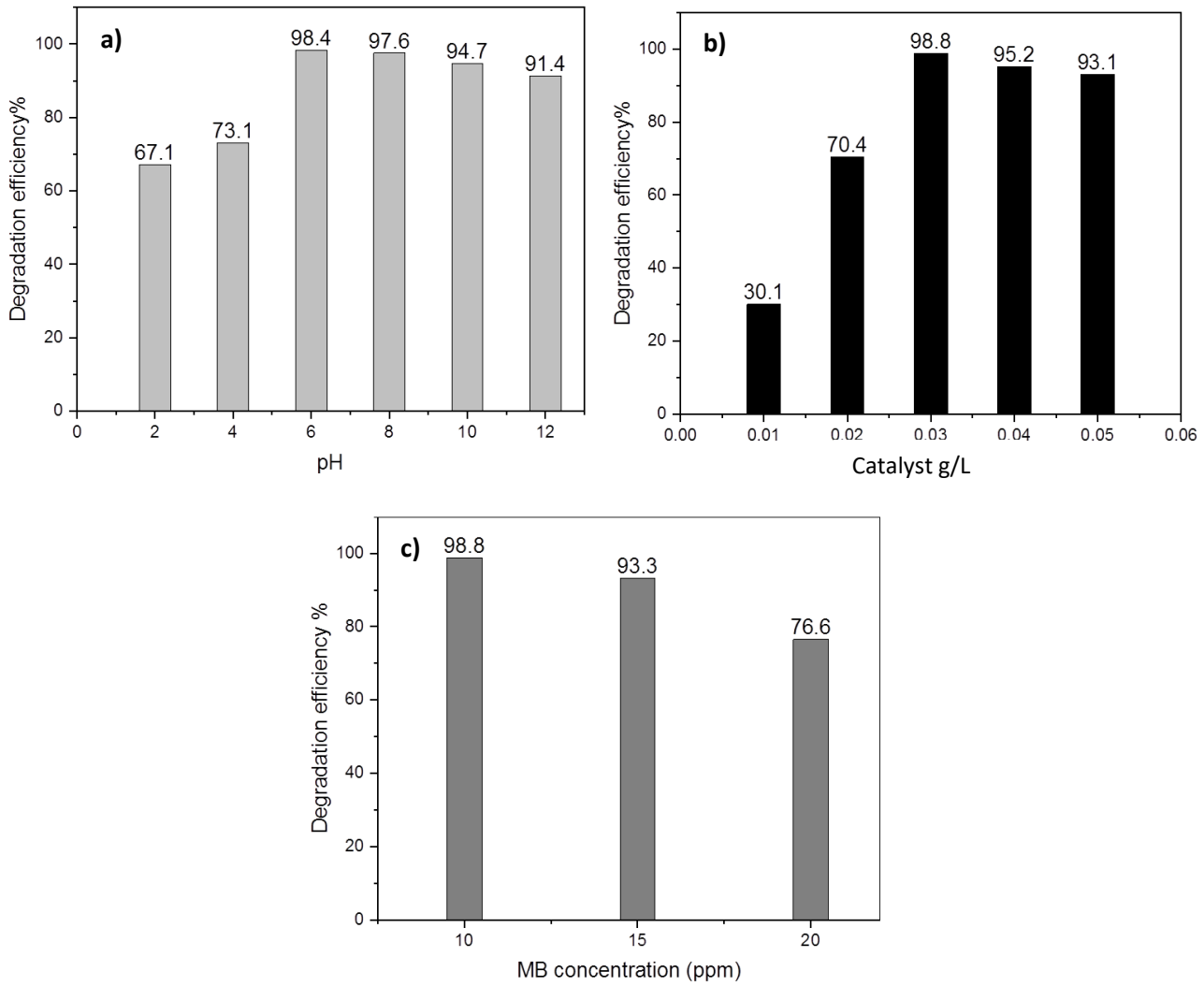

Fig. 12. Effects on MB degradation efficiency of (a) pH (T=25°C, dye concentration = 10 mgL^{-1}, catalyst dose: 0.03 g, and 27 min contact time), (b) catalyst dose (g/L) (T=25°C, dye concentration = 10 mgL^{-1}, pH= 6, and 27 min contact time), and (c) MB concentration (mg/L)) (T=25°C catalyst dose: 0.03 g, pH= 6, and 27 min contact time).

The dye's initial concentration in the wastewater on photocatalytic degradation is a significant factor to consider when assessing the photocatalytic efficiency, so experiments were conducted to investigate the photocatalytic degradation of MB at 10, 15 and 20 mg/L concentrations irradiated with sunlight for 27 min at constant room temperature, with a catalyst dose of 0.03 g/L and a pH value of 6. Fig. 12c demonstrates that as the MB concentration is increased from 10 to 20 ppm, the degradation efficiency decreases from 98.8% to 76.6%. However, higher MB concentrations can scatter or absorb light,

resulting in fewer photons reaching the particle surface, so there are fewer electron-hole pairs generated, resulting in a low photodegradation efficiency. The literature reports analogous trends for organic dye degradation on $CuO/SmFeO_3$ nanocomposite and magnetic $MgFe_2O_4$-$MgTiO_3$ perovskite nanocomposite [81,82].

3.9. Reusability of MFO-CuO/GO nanophotocatalyst

The photocatalyst's reusability and stability are essential factors in determining a photocatalyst's usefulness and industrial validation. Therefore, recyclability experiments for studying the photocatalytic degradation of MB in the presence of MFO-CuO/GO photocatalyst under sunlight were performed while maintaining the other reaction conditions. After the first MB degradation run, the spent MFO-CuO/GO catalyst was collected using an external magnet, washed thoroughly with ethanol and purified water, vacuum dried and utilized for the next measurement. Fig. 13 shows four successive recycling results. After each run, the MB dye degradation efficiency slightly decreased. The slight decline in photocatalyst efficiency may be attributed to adsorption of degradation products on the catalyst surface, blocking some reaction sites and reducing the photocatalytic efficiency. It might also be due to catalyst waste during washing. However, after four cycles, the spent MFO-CuO/GO catalyst still revealed 94.6% degradation efficiency, which indicates excellent stability and reusability; therefore MFO-CuO/GO photocatalyst is a very good candidate for wastewater treatment via photocatalytic degradation process.

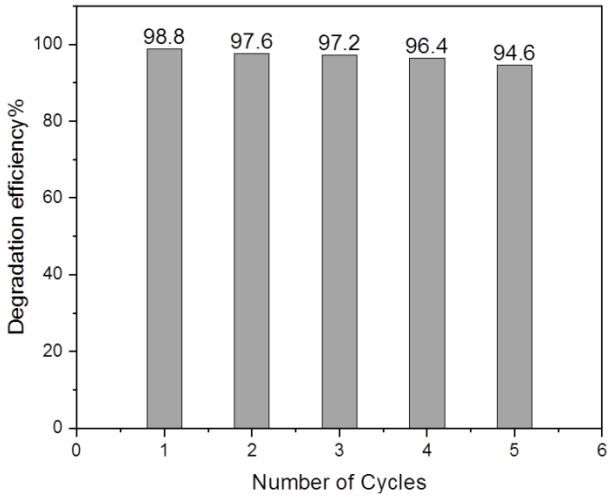

Fig. 13. Reusability of MFO-CuO/GO photocatalyst for MB dye degradation under sunlight irradiation

4. Conclusion

An effective MFO-CuO/GO heterojunction superparamagnetic nanophotocatalyst working under natural sunlight, was successfully synthesized via a microwave-ultrasonic procedure. The characterization by FESEM, TEM, HR-TEM, SAED and XRD techniques confirmed the decoration of graphene nano-sheets with MFO-CuO hybrid semiconductor. The surface investigations indicated that the photocatalyst had a mesoporous structure with a pore volume of 0.0521 $cm^3.g^{-1}$, pore diameter of 2.90 nm and S_{BET} of 96.12 $m^2.g^{-1}$. A batch photocatalytic degradation process was carried out in a glass reactor and optimized in terms of pH, catalyst dose, MB concentration and catalyst reusability. The evaluations revealed greater degradation efficiency (98.8% in 27 min) at pH=6-8, 10 ppm MB concentration, 0.03 g/L catalyst dose, and at least fourfold recyclability. The kinetic studies illustrated a very good rate of photocatalytic degradation of MB dye. The favourable band alignment in our newly engineered heterojunction photocatalyst resulted in effective electron-hole separation, a significant reduction in electron-hole recombination rate, and a large increase in degradation efficiency.

Acknowledgments

The authors greatly appreciate the support provided by the School of Chemical and Pharmaceutical Sciences, Kingston University London. Special gratitude goes to the Dept. of Industrial Chemistry, College of Science and Dept. of Petroleum & Gas Refining Engineering, College of Petroleum Processes Engineering, Tikrit University Iraq.

Declaration of conflicting interests

The author(s) declared no potential conflicts of interest with respect to the research, authorship, and/or publication of this article.

Funding

The author(s) received no financial support for the research, authorship, and/or publication of this article.

ORCID iD

Ibrahim F. Waheed https://orcid.org/0000-0002-8984-1783

Omer Yasin Thayee Al-Janabi https://orcid.org/0000-0001-5435-112X

Peter J. S. Foot https://orcid.org/0000-0002-2122-3129

References

[1] R. Fatima, M.F. Warsi, M.I. Sarwar, I. Shakir, P.O. Agboola, M.F. Aly Aboud and S. Zulfiqar, Synthesis and Characterization of Hetero-metallic Oxides-Reduced Graphene Oxide Nanocomposites for Photocatalytic Applications, Ceramics Int. 47 (2021) 7642-7652. https://doi.org/10.1016/j.ceramint.2020.11.106.

[2] H. Karimi-Maleh, F. Karimi, S. Malekmohammadi, N. Zakariae, R. Esmaeili, S. Rostamnia, M.L. Yola, N. Atar, S. Movaghgharnezhad, S. Rajendran, A. Razmjou, Y. Orooji, S. Agarwal and V.K. Gupta, An amplified voltammetric sensor based on platinum nanoparticle/polyoxometalate/two-dimensional hexagonal boron nitride nanosheets composite and ionic liquid for determination of N-hydroxysuccinimide in water samples, J. Molec. Liq. 310 (2020) 113185. https://doi.org/10.1016/j.molliq.2020.113185 .

[3] H. Karimi-Maleh, B.G. Kumar, S. Rajendran, J. Qin, S. Vadivel, D. Durgalakshmi, F. Gracia, M. Soto-Moscoso, Y. Orooji and F. Karimi, Tuning of metal oxides photocatalytic performance using Ag nanoparticles integration, J. Molec. Liq. 314 (2020) 113588. https://doi.org/10.1016/j.molliq.2020.113588.

[4] H. Karimi-Maleh, M. Shafieizadeh, M.A. Taher, F. Opoku, E.M. Kiarii, P.P. Govender, S. Ranjbari, M. Rezapour and Y. Orooji, The role of magnetite/graphene oxide nano-composite as a high-efficiency adsorbent for removal of phenazopyridine residues from water samples, an experimental/theoretical investigation, J. Molec. Liq. 298 (2020) 112040. https://doi.org/10.1016/j.molliq.2019.112040.

[5] A. Iftikhar, S. Yousaf, F.A. Ahmed Ali, S. Haider, S. Ud-Din Khan, I. Shakir, F. Iqbal and M.F. Warsi, Erbium-substituted $Ni_{0.4}Co_{0.6}Fe_2O_4$ ferrite nanoparticles and their hybrids with reduced graphene oxide as magnetically separable powder photocatalyst, Ceramics Int. 46 (2020) 1203-1210. https://doi.org/10.1016/j.ceramint.2019.08.176.

[6] M. K. Ahmed, M.E. El-Naggar, A. Aldalbahi, M.H. El-Newehy and A. A. Menazea, Methylene blue degradation under visible light of metallic nanoparticles scattered into graphene oxide using laser ablation technique in aqueous solutions, J. Molec. Liq. 315 (2020) 113794. https://doi.org/10.1016/j.molliq.2020.113794.

[7] B. Mandal, J. Panda, P.K. Paul, R. Sarkar and B. Tudu, $MnFe_2O_4$ decorated reduced graphene oxide heterostructures: nanophotocatalyst for methylene blue dye degradation, Vacuum. 173 (2020) 109150. https://doi.org/10.1016/j.vacuum.2019.109150.

[8] A. G. Acedo-Mendoza, A. Infantes-Molina, D. Vargas-Hernández, C.A. Chávez-Sánchez, E. Rodríguez-Castellón and J.C. Tánori-Córdova, Photodegradation of methylene blue and methyl orange with CuO supported on ZnO photocatalysts: The effect of copper loading and reaction

temperature, Mater. Sci. Semiconductor Processing. 119 (2020) 105257. https://doi.org/10.1016/j.mssp.2020.105257.

[9] A.A. Shah, M.A. Bhatti, A. Tahira, A.D. Chandio, I.A. Channa, A.G. Sahito, E. Chalanger, M. Willander, O. Nur and Z.H. Ibupoto, Facile synthesis of copper doped ZnO nanorods for the efficient photo degradation of methylene blue and methyl orange, Ceramics Int. 46 (2020) 9997-10005. https://doi.org/10.1016/j.ceramint.2019.12.024.

[10] K.P. Sapkota, I. Lee, M. Hanif, M. Islam, J. Akter and J.R. Hahn, Enhanced visible-light photocatalysis of nanocomposites of copper oxide and single-walled carbon nanotubes for the degradation of methylene blue, Cataly. 10 (2020) 297. https://doi.org/10.3390/catal10030297.

[11] N. Boudechiche, M. Fares, S. Ouyahia, H. Yazid, M. Trari and Z. Sadaoui, Comparative study on removal of two basic dyes in aqueous medium by adsorption using activated carbon from Ziziphus lotus stones, Microchem. J. 146 (2019) 1010-1018. https://doi.org/10.1016/j.microc.2019.02.010.

[12] M. Daoud, O. Benturki, P. Girods, A. Donnot and S. Fontana, Adsorption ability of activated carbons from Phoenix dactylifera rachis and Ziziphus jujube stones for the removal of commercial dye and the treatment of dyestuff wastewater, Microchem. J. 148 (2019) 493-502. https://doi.org/10.1016/j.microc.2019.05.022.

[13] S. Zereshki, P. Daraei and A. Shokri, Application of edible paraffin oil for cationic dye removal from water using emulsion liquid membrane, J. Hazard. Mater. 356 (2018) 1-8. https://doi.org/10.1016/j.jhazmat.2018.05.037.

[14] Q. Li, T. Zhao, M. Li, W. Li, B. Yang, D. Qin, K. Lv, X. Wang, L. Wu, X. Wu and J. Sun, One-step construction of Pickering emulsion via commercial TiO_2 nanoparticles for photocatalytic dye degradation, Appl. Catal. B . 249 (2019) 1-8. https://doi.org/10.1016/j.apcatb.2019.02.057.

[15] F. Chang, F. Wu, W. Yan, M. Jiao, J. Zheng, B. Deng and X. Hu, Oxygen-rich bismuth oxychloride $Bi_{12}O_{17}Cl_2$ materials: construction, characterization, and sonocatalytic degradation performance, Ultrason. Sonochem. 50 (2019) 105-113. https://doi.org/10.1016/j.ultsonch.2018.09.005.

[16] C. Anushree and J. Philip, Efficient removal of methylene blue dye using cellulose capped Fe_3O_4 nanofluids prepared using oxidation-precipitation method, Colloids Surf. A. 567 (2019) 193-204. https://doi.org/10.1016/j.colsurfa.2019.01.057.

[17] P.V. Nidheesh, M. Zhou and M.A. Oturan, An overview on the removal of synthetic dyes from water by electrochemical advanced oxidation processes, Chemosphere. 197 (2018) 210-227. https://doi.org/10.1016/j.chemosphere.2017.12.195.

[18] Y. Pan, T. Zhu and Z. He, Enhanced removal of azo dye by a electrochemical system integrated with a membrane biofilm reactor, Ind. Eng. Chem. Res. 57 (2018) 16433-16441. https://doi:10.1021/acs.iecr.8b04725.

[19] D. Smazna, S. Shree, O. Polonskyi, S. Lamaka, M. Baum, M. Zheludkevich, F. Faupel, R. Adelung, Y.K. Mishra, Mutual interplay of ZnO micro- and nanowires and methylene blue during cyclic photocatalysis process, J. Environ. Chem. Eng. 7 (2019) 103016. https://doi.org/10.1016/j.jece.2019.103016.

[20] D. Neena, K.K. Kondamareddy, H. Bin, D. Lu, P. Kumar, R.K. Dwivedi, V.O. Pelenovich, X.Z. Zhao, W. Gao and D. Fu, Enhanced visible light photodegradation activity of RhB/MB from aqueous solution using nanosized novel Fe-Cd co-modified ZnO, Sci. Rep. 8 (2018) 1-12. https://doi.org/10.1038/s41598-018-29025-1.

[21] A. Shameem, P. Devendran, V. Siva, M. Raja, S.A. Bahadur and A. Manikandan, Preparation and characterization studies of nanostructured CdO thin films by SILAR method for photocatalytic applications, J. Inorg. Organomet. Polym. Mater. 27 (2017) 692-699. https://doi.org/10.1007/s10904-017-0512-1.

[22] V. Umapathy, P. Neeraja, A. Manikandan and P. Ramu, Synthesis of $NiMoO_4$ nanoparticles by sol-gel method and their structural, morphological, optical, magnetic and photocatlytic properties, Trans. Nonferrous Metals Soc. China 27 (2017) 1785-1793. https://doi.org/10.1016/S1003-6326(17)60201-2.

[23] W. Li, G. Wang, C. Chen, J. Liao and Z. Li, Enhanced visible light photo catalytic activity of ZnO nanowires doped with Mn^{2+} and Co^{2+} ions, Nanomaterials. 7 (2017) 20. https://doi.org/10.3390/nano7010020.

[24] I. Ibrahim, C. Athanasekou, G. Manolis, A. Kaltzoglou,. N.K. Nasikas, F. Katsaros, E. Devlin, A.G. Kontos, P. Falaras, Photocatalysis as an advanced reduction process (ARP): The reduction of 4-nitrophenol using titania nanotubes-ferrite nanocomposites, J. Hazard Mater. 372 (2019) 37-44. https://doi.org/10.1016/j.jhazmat.2018.12.090.

[25] I.F. Waheed, O.Y.T. Al-Janabi, A.K. Ibrahim, P.J.S. Foot, M.A. Alkarawi, B.M. Ali and F.M. Al-Abady, $MgFe_2O_4$/CNTs nanocomposite: synthesis, characterization, and photocatalytic activity, Int. J. Ind. Chem. 11(2020) 13-28. https://doi.org/10.1007/s40090-020-00223-z.

[26] S. Kumar, S.K. Sharma, R.D. Kaushik and L.P. Purohit, Chalcogen-doped zinc oxide nanoparticles for photocatalytic degradation of Rhodamine B under the irradiation of ultraviolet light, Mater. Today Chem. 20 (2021) 100464. https://doi.org/10.1016/j.mtchem.2021.100464.

[27] S. Kumar, R.D. Kaushik, G.K. Upadhyay and L.P. Purohit, rGO-ZnO nanocomposites as efficient photocatalyst for degradation of 4-BP and DEP using high temperature refluxing method in in-situ condition, J. Hazardous Mater. 406 (2021) 124300. https://doi.org/10.1016/j.jhazmat.2020.124300.

[28] R.C. Ngullie, S.O. Alaswad, K. Bhuvaneswari, P. Shanmugam, T. Pazhanivel and P. Arunachalam, Synthesis and Characterization of Efficient ZnO/g-C3N4 Nanocomposites Photocatalyst for Photocatalytic Degradation of Methylene Blue, Coatings. 10 (2020) 500. https://doi.org/10.3390/coatings10050500.

[29] A. Manohar and C. Krishnamoorth, Photocatalytic study and superparamagnetic nature of Zn-doped $MgFe_2O_4$ colloidal size nanocrystals prepared by solvothermal reflux method, J. Photochem. Photobio. B: Biol. 173 (2017) 456-465. https://doi.org/10.1016/j.jphotobiol.2017.06.025.

[30] A.F. Cabrera, C.R. Torres, S.G. Marchetti and S.J. Stewart, Degradation of methylene blue dye under dark and visible light conditions in presence of hybrid composites of nanostructured $MgFe_2O_4$ ferrites and oxygenated organic compounds, J. Environ. Chem. Eng. 8 (2020) 104274. https://doi.org/10.1016/j.jece.2020.104274.

[31] H. Younes, F. Ravaux, N.E. Hadri and L. Zou, Nanostructuring of pseudocapacitive $MnFe_2O_4$/Porous rGO electrodes in capacitive deionization, Electrochim. Acta. 306 (2019) 1-8. https://doi.org/10.1016/j.electacta.2019.03.097.

[32] Y. Yang, J. Liu, B. Zhang and F. Liu, Mechanistic studies of mercury adsorption and oxidation by oxygen over spinel type $MnFe_2O_4$, J. Hazard Mater. 321 (2017) 154-216. https://doi.org/10.1016/j.jhazmat.2016.09.007.

[33] S.M. Alshehri, J. Ahmed, A.N. Alhabarah, T. Ahamad and T. Ahmad, Nitrogen-doped cobalt ferrite/carbon nanocomposites for supercapacitor applications. Chem. ElectroChem. 4 (2017) 2952-2958. https://doi.org/10.1002/celc.201700602.

[34] R. Ciocarlan, E.M. Seftel, M. Mertens, A. Pui, M. Mazaj, N.N. Tusar and P. Cool, Novel magnetic nanocomposites containing quaternary ferrites systems $Co_{0.5}Zn_{0.25}M_{0.25}Fe_2O_4$ (M ¼ Ni, Cu, Mn, Mg) and TiO2-anatase phase as photocatalysts for wastewater remediation under solar light irradiation, Mater. Sci. Eng. B. 230 (2018) 1-7. https://doi.org/10.1016/j.mseb.2017.12.030.

[35] S. Chandrasekaran, C. Bowen, P. Zhang, Z. Li, Q. Yuan, X. Ren and L. Deng, Spinel photocatalysts for environmental remediation, hydrogen generation, CO_2 reduction and photoelectrochemical water splitting, J. Mater. Chem. A. 6 (2018) 11078-11104. https://doi.org/10.1039/C8TA03669A.

[36] L. Zheng, K. Fang, M. Zhang, Z. Nan, L. Zhao, D. Zhou, M. Zhub and W. Li, Tuning of spinel magnesium ferrite nanoparticles with enhanced magnetic properties, RSC. Adv. 8 (2018) 39177-39181. https://doi:10.1039/C8RA07487A.

[37] Y.H. Guan, J. Ma, Y.M. Ren, Y.L. Liu, J.Y. Xiao, L. Lin and C. Zhang, Efficient degradation of atrazine by magnetic porous copper ferrite catalyzed peroxymonosulfate oxidation via the formation of hydroxyl and sulfate radicals, Water Res. 47 (2013) 5431-5438. https://doi.org/10.1016/j.watres.2013.06.023.

[38] Y. Ren, L. Lin, J. Ma, J. Yang, J. Feng and Z. Fan, Sulfate radicals induced from peroxymonosulfate by magnetic ferrospinel MFe_2O_4 (M¼Co, Cu, Mn, and Zn) as heterogeneous catalysts in the water, Appl. Catal. B Environ. 165 (2015) 572-578. https://doi.org/10.1016/j.apcatb.2014.10.051.

[39] M. Stoia, C. Muntean and B. Militaru, $MnFe_2O_4$ nanoparticles as new catalyst for oxidative degradation of phenol by peroxydisulfate, J. Environ. Sci. 53 (2017) 269-277. https://doi.org/10.1016/j.jes.2015.10.035.

[40] X. Wua, W. Wanga, F. Lia, S. Khaimanova, N. Tsidaeva and M. Lahoubi, PEG-assisted hydrothermal synthesis of $CoFe_2O_4$ nanoparticles with enhanced selective adsorption properties for different dyes, Appl. Surf. Sci. 389 (2016) 1003-1011. https://doi.org/10.1016/j.apsusc.2016.08.053.

[41] M. Rahimi-Nasrabadi and M.B.A. Sobhani-Nasab, Nanocrystalline Ce-doped copper ferrite: synthesis, characterization, and its photocatalyst application, J. Mater. Sci. Mater. Electron. 27 (2016) 11691-11697. https://doi.org/10.1007/s10854-016-5305-8.

[42] A. Nadumane, K. Shetty, K.S. Anantharaju, H.P. Nagaswarupa, D. Rangappa, Y.S. Vidya, H. Nagabhushana and S.C. Prashantha, Sunlight photocatalytic performance of Mg-doped nickel ferrite synthesized by a green sol-gel route, J. Sci. Adv. Mater. Devices 4 (2019) 89-100. https://doi.org/10.1016/j.jsamd.2018.12.002.

[43] M.S. Abdel-Wahed, A.S. El-Kalliny, M.I. Badawy, M.S. Attia and T.A. Gad-allah, Core double shell $MnFe_2O_4$@rGO@TiO_2 superparamagnetic photocatalyst for wastewater treatment under solar light, Chem. Eng. J. (2019) 122936. https://doi.org/10.1016/j.cej.2019.122936.

[44] C.H. Nguyen and R.S. Juang, Efficient removal of methylene blue dye by a hybrid adsorption-photocatalysis process using reduced graphene oxide/titanate nanotube composites for water reuse, J. Ind. Eng. Chem. 76 (2019) 296-309. https://doi.org/10.1016/j.jiec.2019.03.054.

[45] J. Ahmed, M. Ubaidullah, T. Ahmad, N. Alhokbany and S.M. Alshehri, Synthesis of graphite oxide/cobalt molybdenum oxide hybrid nanosheets for enhanced electrochemical performance in supercapacitors and the oxygen evolution reaction. Chem. ElectroChem. 6 (2019) 2524-2530. https://doi.org/10.1002/celc.201900055.

[46] M.M. Sabzehmeidani, H. Karimi, M. Ghaedi and V.M. Avargani, Construction of efficient and stable ternary $ZnFe_2O_4$/Ag/AgBr Z-scheme photocatalyst based on $ZnFe_2O_4$ nanofibers under LED visible light, Mater. Res. Bull. 143 (2021) 111449.

https://doi.org/10.1016/j.materresbull.2021.111449.

[47] P.A. Sakhare, S.S. Pawar, T.S. Bhat, S.D. Yadav, G.R. Patil, P.S. Patil and A.D. Sheikh, Magnetically recoverable $BiVO_4/NiFe_2O_4$ nanocomposite photocatalyst for efficient detoxification of polluted water under collected sunlight, Mater. Res. Bull. 129 (2020) 110908. https://doi.org/10.1016/j.materresbull.2020.110908.

[48] M. Sohail, H. Xue, Q. Jiao, H. Li, K. Khan, S. Wang, C. Feng and Y. Zhao, Synthesis of well-dispersed TiO_2/CNTs@ $CoFe_2O_4$ nanocomposites and their photocatalytic properties, Mater. Res. Bull. 101 (2018) 83-89. https://doi.org/10.1016/j.materresbull.2018.01.017.

[49] A. Nezamzadeh-Ejhieh and H. Zabihi-Mobarakeh, Heterogeneous photodecolorization of mixture of methylene blue and bromophenol blue using CuO-nano-clinoptilolite, J. Ind. Eng. Chem. 20 (2014) 1421-1431. https://doi.org/10.1016/j.jiec.2013.07.027.

[50] A.A. Yadav, Y.M. Hunge and S.W. Kang, Spongy ball-like copper oxide nanostructure modified by reduced graphene oxide for enhanced photocatalytic hydrogen production, Mater. Res. Bull. 133 (2021) 111026. https://doi.org/10.1016/j.materresbull.2020.111026.

[51] P. Tancredi, O.M. Londono, P.C.R. Rojas, M. Knobel and L.M. Socolovsky, Step-by-step synthesis of iron-oxide nanoparticles attached to graphene oxide: A study on the composite properties and architecture, Mater. Res. Bull. 107 (2018) 255-263. https://doi.org/10.1016/j.materresbull.2018.08.003.

[52] M.A. Subhan, A.M.M. Fahim, P.C. Saha, M.M. Rahman, K. Begum and A.K. Azad, Structural study, photoluminescence and photocatalytic properties of La_2O_3.Fe_3O_4.ZnO, AgO.NiO.ZnO and La_2O_3.AgO.ZnO nanocomposites, Nano-Structures & Nano-Objects. 10 (2017) 30-41. https://doi.org/10.1016/j.nanoso.2017.03.001.

[53] Z.K. Heiba, M.M.S. Sanad and M.B. Mohamed, Influence of Mg-deficiency on the functional properties of magnesium ferrite anode material, Solid State Ionics. 341 (2019) 115042. https://doi.org/10.1016/j.ssi.2019.115042.

[54] R. Fatima, M. Warsi, S. Zulfiqar, S. Ragab, I. Shakir and M. Sarwar, Nanocrystalline transition metal oxides and their composites with reduced graphene oxide and carbon nanotubes for photocatalytic applications, Ceramics Int. 46 (2020) 16480-16492. https://doi.org/10.1016/j.ceramint.2020.03.213.

[55] Y. Liu, F. Zhang, W. Zhu, D. Su, Z. Sang, X. Yan, S. Li, J. Liang and S.X. Dou, A multifunctional hierarchical porous SiO_2/GO membrane for high efficiency oil/water separation and dye removal, Carbon. 160 (2020) 88-97. https://doi.org/10.1016/j.carbon.2020.01.002.

[56] A.R. Abbasian and M.S. Afarani, One step solution combustion synthesis and characterization of $ZnFe_2O_4$ and $ZnFe_{1.6}O_4$ nanoparticles, Appl. Phys. A. 125 (2019) 1-12.

https://doi.org/10.1007/s00339-019-3017-7.

[57] A.R.B. Bayantong, Y.J. Shih, C.D. Dong, S. Garcia-Segura and M.D.G. de Luna, Nickel ferrite Nano enabled graphene oxide ($NiFe_2O_4$@GO) as photoactive nanocomposites for water treatment, Environ. Sci. Pollut. Res. 28 (2021) 5472-5481. https://doi.org/10.1007/s11356-020-10545-1.

[58] B. Bashir, W. Shaheen, M. Asghar, M.F. Warsi, M.A. Khan, S. Haider, I. Shakir M. and Shahid, Copper doped manganese ferrites nanoparticles anchored on graphene nano-sheets for high performance energy storage applications, J. Alloys Comp. 695 (2017) 881-887. https://doi.org/10.1016/j.jallcom.2016.10.183.

[59] L.T.T. Nguyen, L.T. Nguyen, N.C. Manh, D.N. Quoc, H.N. Quang, H.T. Nguyen, D.C. Nguyen, L.G. Bach, A facile synthesis, characterization, and photocatalytic activity of magnesium ferrite nanoparticles via the solution combustion method, J. Chem. 2019 (2019). https://doi.org/10.1155/2019/3428681.

[60] S.T. Fardood, Z. Golfar and A. Ramazani, Novel sol-gel synthesis and characterization of superparamagnetic magnesium ferrite nanoparticles using tragacanth gum as a magnetically separable photocatalyst for degradation of reactive blue 21 dye and kinetic study, J. Mater. Sci. Mater. Electron. 28 (2017) 17002-17008. https://doi.org/10.1007/s10854-017-7622-y.

[61] K.R. Reddy, Green synthesis, morphological and optical studies of CuO nanoparticles, J. Mol. Struct. 1150 (2017) 553-557. https://doi.org/10.1016/j.molstruc.2017.09.005.

[62] B. Kirubasankar, V. Murugadoss and S. Angaiah, Hydrothermal assisted in situ growth of CoSe onto graphene nanosheets as a nanohybrid positive electrode for asymmetric supercapacitors, RSC. Adv. 7 (2017) 5853-5862. https://doi.org/10.1039/C6RA25078E.

[63] B. Kirubasankar, V. Murugadoss, J. Lin, T. Ding, M. Dong, H. Liu, J. Zhang, T. Li, N. Wang, Z. Guo and S. Angaiah, In situ grown nickel selenide on graphene nanohybrid electrodes for high energy density asymmetric supercapacitors, Nanoscale. 10 (2018) 20414-20425. https://doi.org/10.1039/C8NR06345A.

[64] L. Chen, D. Ding, C. Liu, H. Cai, Y. Qu, S. Yang, Y. Gao and T. Cai, Degradation of norfloxacin by $CoFe_2O_4$-GO composite coupled with peroxymonosulfate: a comparative study and mechanistic consideration, Chem. Eng. J. 334 (2018) 273-284. https://doi.org/10.1016/j.cej.2017.10.040.

[65] A. Modwi, M.A. Abbo, E.A. Hassan, O.K. Al-Duaij and A. Houas, Adsorption kinetics and photocatalytic degradation of malachite green (MG) via Cu/ZnO nanocomposites, J. Environ. Chem. Eng. 5 (2017) 5954-5960. https://doi.org/10.1016/j.jece.2017.11.024.

[66] L.A. Kafshgari, M. Ghorbani and A. Azizi, Fabrication and investigation of $MnFe_2O_4$/MWCNTs nanocomposite by hydrothermal technique and adsorption of cationic and anionic dyes, Appl. Surf. Sci. 419 (2017) 70-83. https://doi.org/10.1016/j.apsusc.2017.05.019.

[67] P. Nuengmatcha, P. Porrawatkul, S. Chanthai, P. Sricharoen and N. Limchoowong, Enhanced photocatalytic degradation of methylene blue using Fe_2O_3/graphene/CuO nanocomposites under visible light, J. Environ. Chem. Eng. 7 (2019) 103438. https://doi.org/10.1016/j.jece.2019.103438.

[68] Z. Zhu, C. Wang, L. Liang D. Yu J. Sun, L. Zhang, S. Zhong and B. Liu, Synthesis of novel ternary photocatalyst Ag_3PO_4/Bi_2WO_6/Multi-Walled Carbon nanotubes and its enhanced visible-light photoactivity for photodegradation of norfloxacin, J. Nanosci. Nanotechnol. 20 (2020) 2247-2258. https://doi.org/10.1166/jnn.2020.17368.

[69] E. Thimsen, S. Biswas, C.S. Lo and P. Biswas, Predicting the band structure of mixed transition metal oxides: theory and experiment, J. Phys. Chem. C. 113 (2009) 2014-2021. https://doi.org/10.1021/jp807579h.

[70] V. Sharma and R.C. Prajapati, Synthesis of mixed metal oxide nanoparticles of SnO_2 with SrO via sol-gel technology: their structural, optical, and electrical properties, J. Sol. Gel Sci. Technol. 87 (2018) 41-49. https://doi.org/10.1007/s10971-018-4718-7.

[71] S. Kumar, R.D. Kaushik and L.P. Purohit, Hetro-nanostructured Se-ZnO sustained with RGO nanosheets for enhanced photocatalytic degradation of p-Chlorophenol, p-Nitrophenol and Methylene blue, Sep. Purif. Technol. 275 (2021) 119219. https://doi.org/10.1016/j.seppur.2021.119219.

[72] G. Panthi, K.R. Gyawali and M. Park, Towards the Enhancement in Photocatalytic Performance of Ag_3PO_4 Nanoparticles through Sulfate Doping and Anchoring on Electrospun Nanofibers, Nanomaterials, 10 (2020) 929. https://doi.org/10.3390/nano10050929.

[73] G. Panthi, O.H. Kwon, Y.S. Kuk, K.R. Gyawali, Y.W. Park and M. Park, Ternary Composite of Co-Doped CdSe@ electrospun Carbon Nanofibers: A Novel Reusable Visible Light-Driven Photocatalyst with Enhanced Performance, Catalysts. 10 (2020) 348. https://doi.org/10.3390/catal10030348.

[74] L. Jiang, X. Yuan, G. Zeng, J. Liang, X. Chen, H. Yu, H. Wang, Z. Wu Z, J. Zhang and T. Xiong, In-situ synthesis of direct solid-state dual Z-scheme WO_3/g-C_3N_4/Bi_2O_3 photocatalyst for the degradation of refractory pollutant, Appl. Catal. B: Environ. 227 (2018) 376-385. https://doi.org/10.1016/j.apcatb.2018.01.042.

[75] S. Kumar, R.D. Kaushik and L.P. Purohit, Novel ZnO tetrapod-reduced graphene oxide nanocomposites for enhanced photocatalytic degradation of phenolic compounds and MB dye, J. Molec. Liquids. 327 (2021) 114814. https://doi.org/10.1016/j.molliq.2020.114814.

[76] T. Tachikawa, M. Fujitsuka and T. Majima, Mechanistic insight into the TiO_2 photocatalytic reactions: design of new photocatalysts, J. Phys. Chem. C. 111 (2007) 5259-5275. https://doi.org/10.1021/jp069005u.

[77] S. Kumar, R.D. Kaushik and L.P. Purohit, ZnO-CdO nanocomposites incorporated with graphene

oxide nanosheets for efficient photocatalytic degradation of bisphenol A, thymol blue and ciprofloxacin, J. Hazardous Mater. 424 (2022) 127332. https://doi.org/10.1016/j.jhazmat.2021.127332.

[78] A. Kalam, A. Al-Sehemi, M. Assiri, G. Du, T. Ahmad, I. Ahmad and M. Pannipara, Modified solvothermal synthesis of cobalt ferrite (CoFe2O4) magnetic nanoparticles photocatalysts for degradation of methylene blue with H_2O_2/visible light. Results in physics, 8 (2018) 1046-1053) https://doi.org/10.1016/j.rinp.2018.01.045.

[79] A. Mehtab, J. Ahmed, S.M. Alshehri, Y. Mao and T. Ahmad, Rare earth doped metal oxide nanoparticles for photocatalysis: a perspective. Nanotech. 33 (2021) 142001. https://doi.org/10.1088/1361-6528/ac43e7.

[80] T. Nguyen, T. Thu, N.N. Thi, V.T. Quang and K. Nguyen, Synthesis, characterisation and effect of pH on degradation of dyes of copper-doped TiO_2, J. Exp. Nanosci. 11 (2016) 226-238, https://doi.org/10.1080/17458080.2015.1053541.

[81] Z. Behzadifard, Z. Shariatinia and M. Jourshabani, Novel visible light driven CuO/$SmFeO_3$ nanocomposite photocatalysts with enhanced photocatalytic activities for degradation of organic pollutants, J. Mol. Liq. 262 (2018) 533-548. https://doi.org/10.1016/j.molliq.2018.04.126.

[82] A. Kiani, G. Nabiyouni, S. Masoumi and D. Ghanbari, A novel magnetic $MgFe_2O_4$-$MgTiO_3$ perovskite nanocomposite: Rapid photo-degradation of toxic dyes under visible irradiation, Composites Part B. Eng. 175 (2019) 107080. https://doi.org/10.1016/j.compositesb.2019.107080.